Efficient Processing for Far-From-Transmitter Formation-Flying SAR Receivers

Gerardo Di Martino, *Senior Member, IEEE*, Alessio Di Simone, *Member, IEEE*, Antonio Iodice, *Senior Member, IEEE*, Daniele Riccio, *Fellow, IEEE*, and Giuseppe Ruello, *Senior Member, IEEE*

***Abstract*— In the framework of passive multistatic radars, formation-flying synthetic aperture radar (FF-SAR) represents an intriguing remote sensing solution due to the enhanced imaging capabilities with respect to the conventional SAR. In this article, we focus on FF-SAR systems operating in a far-from-transmitter geometry, developing a signal model suited to this specific configuration. Additionally, we present an efficient processing scheme that, by properly combining the received raw echoes in a coherent fashion, enables two peculiar imaging modes of FF-SAR, namely, signal-to-noise ratio (SNR) improvement and high-resolution wide swath (HRWS). Simulation results show that achieved radiometric and geometric imaging performances are in line with those offered by an equivalent monostatic SAR. In HRWS imaging mode, azimuth ambiguity suppression and SNR improve as the number of satellites increases and are maximized by specific receivers along-track baselines, whose expression is provided. Finally, we present a statistical analysis of the processing performance parameters for random receivers' positions, both assuming a fixed pulse repetition frequency (PRF) and allowing for an adaptive PRF tuning. This last analysis is also directly applicable to clusters of SAR receivers not far from the transmitter.**

***Index Terms*— Bistatic synthetic aperture radar (SAR), distributed SAR, formation-flying SAR (FF-SAR), high-resolution wide swath (HRWS), signal-to-noise ratio (SNR).**

NOMENCLATURE

Symbol	Description
x, r, and ϑ	Azimuth, range, and look angle coordinates.
r_0 and ϑ_0	Range and look angle at the range swath center.
d	Along-track distance between transmitter and receiver formation center.
Δx_n	Azimuth position of the nth receiver with respect to the formation center.
X_{T}	Azimuth footprint of the transmitted beam.
S_{WT}	Slant range swath of the transmitted beam.
b_{R}	Radius of the cylinder enclosing the formation.
l_{R}	Overall along-track length of the receiver formation.
v	Velocity of the transmitter and the receiver formation.
PRF	Pulse repetition frequency.
$\psi(r)$	Receiver formation center squint angle.
$\cos\psi$, $\sin\psi$	See (5).
$\Delta\bar{x}_n(r)$	nth receiver equivalent phase center shift, see (7).
$\beta(r)$	See (7).
$\alpha(r)$	See (8).
$\Delta r_{cn}(x,r)$	Cross-track baseline term, see (9).
$\Delta r_{an}(x,r)$	Along-track baseline term, see (10).
r'	See (12).
x'	vt (transmitter position at time t).
$\Delta\dot{r}_{an}$	Range derivative of Δr_{an} at $r = r'$, see (16).
$\Delta\dot{r}_{cn}$	Range derivative of Δr_{cn} at $r = r'$, see (19).
η_{0n}	nth receiver spectral range shift, see (25).
$a(r)$	See (31).
ξ_{s}	$2\pi\mathrm{PRF}/v$.
ξ_{DC}	Spectral azimuth shift (Doppler centroid), see (34).
$\Delta\bar{x}_{0n}$, α_0, a_0, ψ_0	Values of $\Delta\bar{x}_n$, α, a, and ψ evaluated at $r = r_0$.

Manuscript received 28 July 2022; revised 19 October 2022 and 6 April 2023; accepted 19 June 2023. Date of publication 30 June 2023; date of current version 14 July 2023. This work was supported by the Italian Ministry of University and Research through the Project "FORmation Flying of CubEsat Assemblies for Remote Sensing (FORCE)." *(Corresponding author: Alessio Di Simone.)*

The authors are with the Department of Electrical Engineering and Information Technology, University of Naples Federico II, 80125 Napoli, Italy, and also with Consorzio Nazionale Interuniversitario per le Telecomunicazioni-Laboratorio Nazionale di Comunicazioni Multimediali, Complesso Universitario di Monte S. Angelo, 80126 Napoli, Italy (e-mail: gerardo.dimartino@unina.it; alessio.disimone@unina.it; iodice@unina.it; daniele.riccio@unina.it; ruello@unina.it).

Digital Object Identifier 10.1109/TGRS.2023.3290946

I. INTRODUCTION

SPACEBORNE synthetic aperture radar (SAR) is a mature remote sensing technology exploited for both Earth observation and planetary explorations since the early 1990s [1], [2], [3]. In the last two decades, two complementary paradigms dictated the development of spaceborne SAR missions: on the one hand, very-high-resolution SAR systems, such as COSMO-SkyMed, TerraSAR-X, and RADARSAT-2, were deployed to support Earth observation with unprecedented spatial resolution and moderate range swath; on the other hand, mid-resolution spaceborne missions, such as Sentinel-1, provide coverage at much larger scales with limited

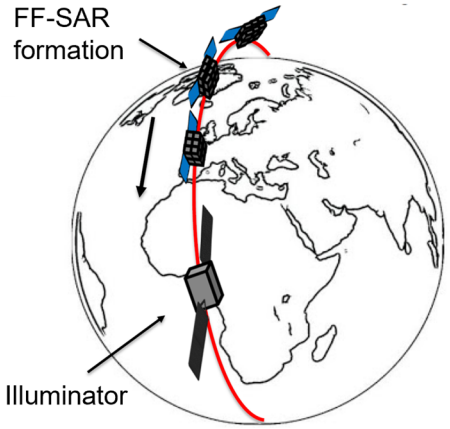

Fig. 1. Pictorial view of an FF-SAR system.

spatial resolution. Such trends reflect one of the intrinsic limitations of monostatic SAR, namely, the tradeoff between azimuth spatial resolution and range swath size, due to the Nyquist sampling limit: a wider coverage can be achieved at the cost of a worse spatial resolution.

Formation-flying SAR (FF-SAR) refers to a distributed multistatic SAR where a cluster of receiving satellites orbiting in coordinated motion acquires the frequency-modulated signal emitted from an SAR transmitter which is either part of the cluster itself or opportunistically exploited [4] (see Fig. 1). The receiving platforms are designed to cooperatively form a single multistatic SAR image, which is obtained by coherently integrating the signals received by each satellite. The receiving cluster can exhibit an along-track and/or a cross-track baseline, which is exploited to improve the imaging performance of monostatic SAR or to implement innovative acquisition modes. As a matter of fact, FF-SAR represents a generalization of conventional monostatic SAR, where the multistatic geometry enables new and more complex imaging modes with respect to traditional SAR. A partial list of possible imaging modalities offered by FF-SAR is given as follows [5].

1) *Signal-to-Noise Ratio (SNR) Improvement [6], [7]*: The coherent combination of the signals received by the whole formation can be exploited to reduce the thermal noise power.
2) *High-Resolution Wide Swath (HRWS) [8], [9]*: Range swath is increased by reducing the transmitter PRF below the Nyquist limit and, therefore, avoiding azimuth resolution degradation. Resulting azimuth ambiguities can be suppressed via proper spectrum reconstruction approaches. Such an imaging mode cannot be implemented with the conventional monostatic SAR and requires an along-track separation between the receiving antennas.
3) *Coherent Resolution Enhancement (CRE) [10], [11]*: A cross-track baseline between receivers can be exploited to improve range resolution via a coherent weighted combination of the spectrum of the received signals.
4) *SAR Interferometry and Tomography [12], [13]*: An FF-SAR system can implement single-pass interferometry and 3-D reconstruction by properly positioning the receiving formation. This can avoid the detrimental effects of temporal decorrelation of repeat-pass interferometry on 3-D products.
5) *Ground Moving Target Indication (GMTI) [11], [14]*: A cluster of receiving platforms with an along-track separation might be fruitfully exploited to support an accurate clutter suppression in GMTI applications.

As it is clear, the development of data synthesis algorithms is of paramount importance for an appropriate coherent combination of the signals received by the FF-SAR cluster and, hence, for addressing in a quantitative way the potentialities of FF-SAR as a remote sensing technology.

In this work, we address data synthesis for FF-SAR and its imaging capabilities. To this end, we focus on the SNR improvement and HRWS imaging modes, which are of particular interest in envisioned FF-SAR missions [15].

We relax the usually made assumption of a sufficiently small transmitter-to-receiver baseline (see [16], [17], [18], [19]), thus focusing on far-from-transmitter (FfT) acquisition geometries, where the receiver formation center squint angle is no longer negligible. We derive an analytical formulation of the echoes received by the N-sat formation and of the FF-SAR transfer function. Additionally, we develop a three-step processing scheme, stemming from the proposed signal model, and based on the coherent combination of the received signals to support noise suppression and azimuth ambiguity removal when sensor PRF is below the Nyquist limit. Finally, we assess the performance of the algorithm by both an original theoretical/statistical analysis of proper performance parameters and by numerical simulations.

We explicitly note that the practical implementation of FF-SAR systems also requires facing time and phase synchronization issues [20], [21], [22]. They are beyond the scope of this article, but we underline that in the FfT case, they can be analyzed and taken under control, in the same way as in the non-FfT case of [20], [21], and [22].

The remainder of this article is organized as follows. Section II describes the received signal model for FfT FF-SAR. Section III discusses the data synthesis approach suited to the derived signal model and to both SNR improvement and HRWS acquisition modes. Section IV is devoted to performance assessment under theoretical, statistical, and simulation respects. Concluding remarks and future research lines are highlighted in Section V.

II. Signal Model

The considered FfT-FF-SAR geometry is schematically depicted in Fig. 2: one transmitter and N receivers move approximately on the same track with constant velocity v. The transmitter operates in stripmap mode, and the azimuth footprint of the transmitted beam is X_{T}, while the slant range swath is S_{WT}. We assume that the receivers' antennas are pointed toward the illuminated scene and their beams are wider

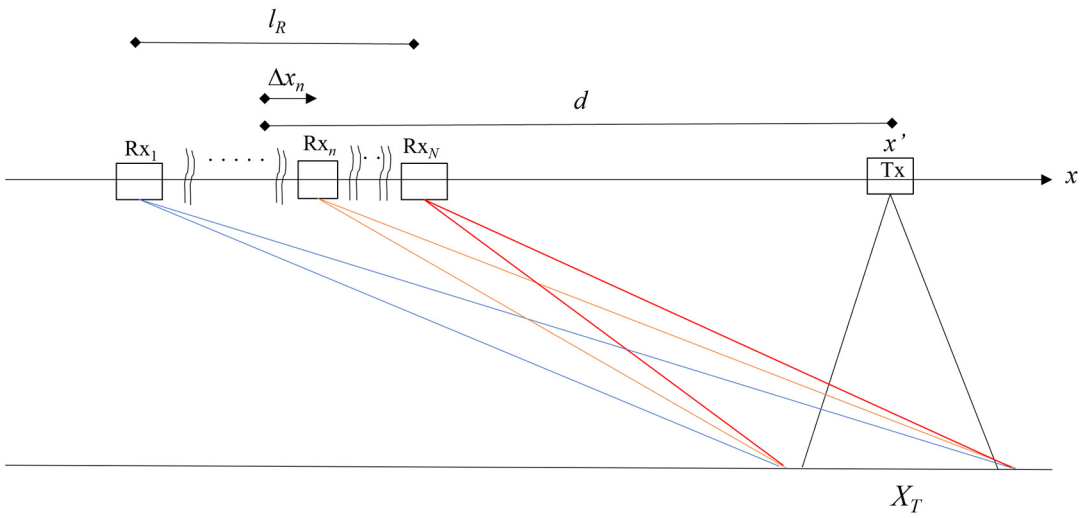

Fig. 2. FfT-FF-SAR schematic view.

than the one of the transmitting antenna, so that their footprints include the illuminated area. We also assume that the relative positions and attitudes of all satellites can be considered constant during the acquisition time. These assumptions are reasonable from an astronautical viewpoint (see [23]).

We use a cylindrical coordinate system x, r, ϑ, whose axis, labeled as x, is the transmitter line of flight (i.e., the azimuth direction) and whose polar angle ϑ is defined with respect to the vertical direction (i.e., it is the look angle) (see Fig. 3); the r coordinate is the distance from the line of flight (i.e., the slant range). The transmitter position at time t is Tx $\equiv (x', 0, 0)$, with $x' = vt$; the receivers formation follows the transmitter at an along-track distance d, so that the formation center is Rx $\equiv (x_{\mathrm{R}}', 0, 0)$, with $x_{\mathrm{R}}' = x' - d$; and the nth receiver position is $\mathrm{Rx}_n \equiv (x_{\mathrm{R}n}', b_n, \vartheta_n)$, with $x_{\mathrm{R}n}' = x' - d + \Delta x_n$ and $n = 1, \ldots, N$. Accordingly, Δx_n and b_n are the along-track and cross-track baselines of the nth receiver with respect to the formation center, respectively (see Fig. 3). The overall along-track length of the receiver formation is $l_{\mathrm{R}} = x_{\mathrm{R}N}' - x_{\mathrm{R}1}' = \Delta x_N - \Delta x_1 = 2\Delta x_N = 2|\Delta x_1|$, so that $|\Delta x_n| \leq l_{\mathrm{R}}/2$, and the receivers are enclosed in a tube of axis x and radius b_{R}, so that $b_n \leq b_{\mathrm{R}}$.

The generic ground point is $P \equiv (x, r, \vartheta(x, r))$, where $\vartheta(x, r)$ describes the terrain height profile. The range swath center is at $r = r_0$ and $\vartheta = \vartheta_0$.

We assume that l_{R}, b_{R}, and X_{T} are much smaller than r, whereas d may be as large as about $r/4$. In addition, we assume that b_{R} is much smaller than l_{R} and X_{T}.

The transmitter emits chirp pulses $p(t - t_i)$ at times $t_i = i/\mathrm{PRF}$, where PRF is the pulse repetition frequency. The carrier frequency and bandwidth of the pulses are f_{c} and Δf, respectively. Transmitter positions at times of pulse transmission are $x_i' = vt_i$.

A. Space Domain

By applying the usual stop-and-start approximation [1], the signal at the nth receiver, after demodulation and chirp pulse compression, can be written as

$$s_n(x_i', t - t_i) = \int\int \gamma(x, r) g_n(x_i' - x, t - t_i; r) dx dr \quad (1)$$

where $\gamma(x, r)$ is the ground point bistatic reflectivity

$$g_n(x_i' - x, t - t_i; r) = \exp\left[-j\frac{2\pi}{\lambda}(r_T + r_n)\right] \mathrm{sinc}\left[\pi \Delta f \left(t - t_i - \frac{r_T + r_n}{c}\right)\right] w\left(\frac{x_i' - x}{X_T}\right). \quad (2)$$

c is the speed of light, $\lambda = c/f_{\mathrm{c}}$ is the wavelength, $w(\cdot)$ is the product of the transmitting and receiving antenna azimuth patterns, which is assumed approximately unitary if the modulus of its argument is smaller than 0.5 and negligible otherwise, and r_{T} and r_n are the distances of the ground point from the transmitter and from the nth receiver, respectively (see Fig. 3). These distances can be computed as (3) and (4), shown at the bottom of the next page, where

$$\cos\psi = \frac{r}{\sqrt{r^2 + d^2}} \quad \text{and} \quad \sin\psi = \frac{d}{\sqrt{r^2 + d^2}}. \quad (5)$$

ψ being the receiver formation center squint angle (see Fig. 3). In (5), and in the following of this section, we provisionally treat x_i' as a continuous variable of x'. Sampling issues will be dealt with in Section II-B. After some algebraic manipulation (see Appendix A), we get

$$r_T + r_n \cong \alpha(r) r + \Delta r_{cn}(x, r) + \Delta r_{an}(r) + \Delta R_n\left(r, x' - x + \Delta \bar{x}_n(r)\right) \quad (6)$$

where

$$\Delta \bar{x}_n(r) = \frac{\cos^3\psi(r)}{\beta(r)} \Delta x_n, \quad \text{with } \beta(r) = 1 + \cos^3\psi(r) \quad (7)$$

is the equivalent phase center shift

$$\alpha(r) = \frac{1 + \cos\psi(r)}{\cos\psi(r)} \quad (8)$$

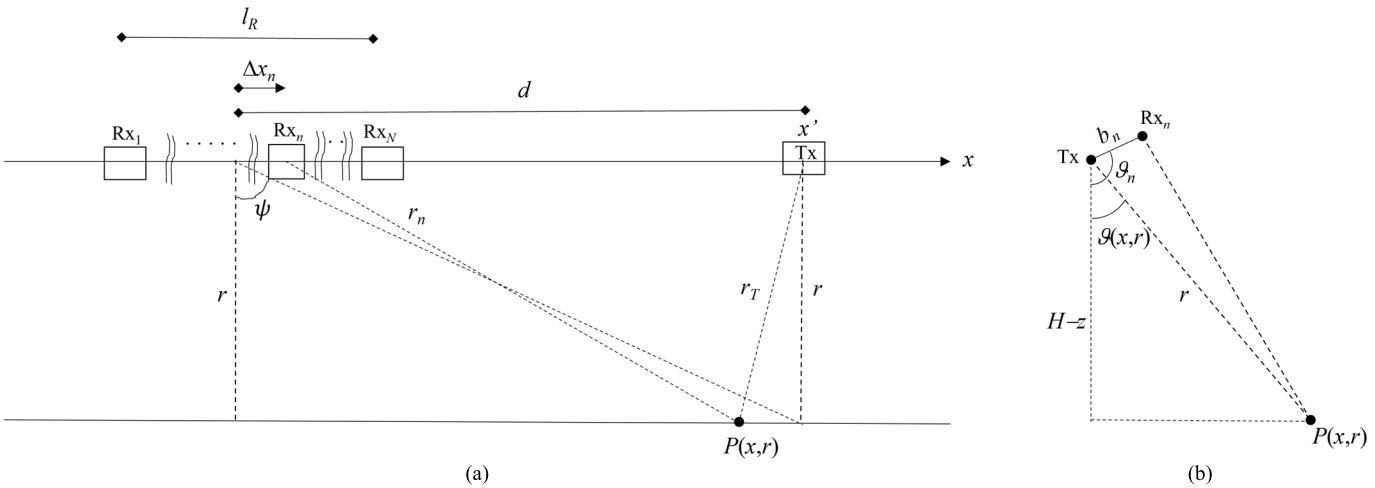

Fig. 3. FfT-FF-SAR geometry. (a) Frontal view and (b) lateral view.

so that αr is the bistatic range term identical for all receivers

$$\Delta r_{cn}(x,r) = -\cos\psi(r) b_n \cos(\vartheta_n - \vartheta(x,r)) \tag{9}$$

is the cross-track baseline term

$$\Delta r_{an}(r) = -\frac{\sin\psi(r)}{\beta(r)}\Delta x_n + \frac{\cos^3\psi(r)}{\beta(r)}\frac{\Delta x_n^2}{2r} \tag{10}$$

is the along-track baseline term, and finally

$$\begin{aligned}&\Delta R_n\left(r, x' - x + \Delta\bar{x}_n(r)\right)\\ &= -\sin\psi(r)\left(x' - x + \Delta\bar{x}_n(r)\right) + \frac{\beta(r)}{2r}\left(x' - x + \Delta\bar{x}_n(r)\right)^2\end{aligned} \tag{11}$$

is the term responsible for azimuth frequency modulation and range migration in the nth receiver raw signal.

By letting

$$r' = \frac{c}{\alpha_0}(t - t_i) \tag{12}$$

with $\alpha_0 = \alpha(r_0)$, and substituting (6) and (12) into (1) and (2), we obtain

$$s_n\left(x', r'\right) = \int\int \gamma(x,r) g_n\left(x' - x, r' - r; r\right) dx dr \tag{13}$$

with

$$\begin{aligned}g_n\left(x' - x, r' - r; r\right) \cong \exp\left[-j\frac{2\pi}{\lambda}\left(\Delta r_{cn} + \Delta r_{an} + \Delta R_n\right)\right]\cdot\\ \cdot \operatorname{sinc}\left[\frac{\pi\alpha_0\Delta f}{c}\left(r' - r - \frac{\Delta r_{cn} + \Delta r_{an} + \Delta R_n}{\alpha_0}\right)\right] w\left(\frac{x' - x}{X_T}\right)\end{aligned} \tag{14}$$

where the phase term $\exp(-j2\pi\alpha r/\lambda)$, which only depends on r and is the same for all receivers, has been included in $\gamma(x,r)$.

Some considerations are now in order. First of all, if $d = 0$, then $\sin\psi = 0$, $\cos\psi = 1$, $\alpha = \beta = 2$, and $\Delta\bar{x}_n = \Delta x_n/2$, so that we recover the expressions already available in [16], [17], [18], and [19]. Conversely, if d is smaller, but not much smaller, than r, the effect of the squint angle ψ cannot be neglected since variations of distance terms of the order of wavelength (i.e., centimetric) significantly affect the argument of the exponential in (14). In addition, in this case ψ, and hence Δr_{an}, are slightly dependent on r. Considering that the difference between r and r' is limited by the presence of the sinc function in (14), we can perform the first-order expansion of Δr_{an} around r'

$$\Delta r_{an}(r) \cong \Delta r_{an}\left(r'\right) + \Delta\dot{r}_{an}\cdot\left(r - r'\right) \tag{15}$$

where (see Appendix B)

$$\Delta\dot{r}_{an} = \left.\frac{d\Delta r_{an}}{dr}\right|_{r=r'} \cong \sin\psi\cos^2\psi\frac{\Delta x_n}{\beta r'} \cong \frac{d}{r_0^2 + d^2}\frac{\Delta x_n}{2}. \tag{16}$$

$$r_T = \sqrt{r^2 + (x' - x)^2} \cong r + \frac{\left(x' - x\right)^2}{2r} \tag{3}$$

$$\begin{aligned}r_n &= \sqrt{r^2 - 2rb_n\cos(\vartheta_n - \vartheta) + b_n^2 + (x' - d + \Delta x_n - x)^2} =\\ &= \sqrt{r^2 + d^2 - 2rb_n\cos(\vartheta_n - \vartheta) + b_n^2 - 2d(x' - x + \Delta x_n) + (x' - x + \Delta x_n)^2}\\ &\cong \frac{r}{\cos\psi} - \sin\psi\left(x' - x + \Delta x_n\right) + \cos^3\psi\frac{\left(x' - x + \Delta x_n\right)^2}{2r} - \cos\psi b_n\cos(\vartheta_n - \vartheta)\end{aligned} \tag{4}$$

Similarly, we can perform the first-order expansion of the cross-track baseline term Δr_{cn}, around (r', x'), so obtaining (see Appendix B)

$$\Delta r_{cn}(x,r) \cong \Delta r_{cn}(x',r') + - \cos\psi(r_0)\frac{b_n \sin(\vartheta_n - \vartheta_0)}{r_0 \tan\vartheta_0}\left[(r-r') + \frac{z(x,r') - z(x',r')}{\cos\vartheta_0}\right] \tag{17}$$

where $z(x,r)$ is the ground-point height over the sea level. The second term in the square brackets of (17), including terrain height variations, is negligible (i.e., much smaller than λ) if $b_R \Delta z/(\lambda r_0)$ is much smaller than one, where Δz is the maximum terrain height variation within one azimuth footprint X_T. For Δz of the order of 100 m and a typical X-band FF-SAR system ($\lambda \cong 3 \times 10^{-2}$ m and $r_0 \cong 6 \times 10^5$ m), this corresponds to b_R not larger than about 20 m. In this case, we can rewrite (17) as

$$\Delta r_{cn}(x,r) \cong \Delta r_{cn}(x',r') + \Delta \dot{r}_{cn} \cdot (r-r') \tag{18}$$

where

$$\Delta \dot{r}_{cn} \cong -\cos\psi(r_0)\frac{b_n \sin(\vartheta_n - \vartheta_0)}{r_0 \tan\vartheta_0}. \tag{19}$$

We also assume that the r-dependence of ψ and ϑ in the argument of the sinc function can be completely neglected because it leads to variations of the distance terms small with respect to the range resolution $c/(\alpha\Delta f) \cong c/(2\Delta f)$. This assumption is valid if [see (16) and (19)]

$$\frac{1}{8}\frac{dl_R S_{WT}}{r_0^2} \ll \frac{c}{2\Delta f} \text{ and } \frac{b_R S_{WT}}{2r_0} \ll \frac{c}{2\Delta f}. \tag{20}$$

Finally, we assume that the r-dependence of $\Delta\bar{x}_n$ can be ignored, too, because it leads to variations of $\Delta\bar{x}_n$ small with respect to the azimuth resolution. By using the expression of the range derivative of $\Delta\bar{x}_n$ computed in (73), we conclude that the condition above is satisfied if

$$\frac{3}{16}\frac{d^2 l_R}{r_0^3} S_{WT} \ll \frac{L}{2}. \tag{21}$$

Based on the considerations above, (13) and (14) can be rewritten as

$$s_n(x',r') = \exp\left\{-j\frac{2\pi}{\lambda}\left[\Delta r_{cn}(x',r') + \Delta r_{an}(r')\right]\right\} s'_n(x',r') \tag{22}$$

where

$$s'_n(x',r') = \int\int \gamma(x,r) g'_n(x'-x, r'-r; r)\, dx\, dr \tag{23}$$

with

$$g'_n(x'-x, r'-r; r) = \exp\left[j\eta_{0n}\cdot(r'-r)\right]\exp\left(-j\frac{2\pi}{\lambda}\Delta R_n\right) \cdot \operatorname{sinc}\left[\frac{\pi\alpha_0\Delta f}{c}\left(r'-r-\frac{\Delta r_{cn}+\Delta r_{an}+\Delta R_n}{\alpha_0}\right)\right] w\left(\frac{x'-x}{X_T}\right) \tag{24}$$

and

$$\eta_{0n} = \frac{2\pi}{\lambda}\left(\Delta\dot{r}_{cn} + \Delta\dot{r}_{an}\right). \tag{25}$$

Finally, we recall that a thermal noise $n_n(x',r')$ is added to the signal of (22) so that the actually measured signal at the nth receiver is

$$\hat{s}_n(x',r') = s_n(x',r') + n_n(x',r'). \tag{26}$$

We assume that noises at different receivers are independent and all have the same statistics.

B. Fourier Domain

By performing the 2-D Fourier transform (FT) of (23), and after a stationary-phase evaluation of the Fourier integral, we get

$$S'_n(\xi,\eta) = D(\xi,\eta) H_n(\xi,\eta) \tag{27}$$

where the angular spatial frequencies ξ and η are the Fourier mates of x' and r', respectively,

$$D(\xi,\eta) = \iint \gamma(x,r) G(\xi,\eta;r)\exp(-j\xi x - j\eta r)\, dx\, dr \tag{28}$$

is the FT of the raw signal of an equivalent monostatic SAR, with

$$G(\xi,\eta;r) \cong \exp\left\{ j\left[\frac{\xi^2}{4a\left(1+\frac{\eta\lambda}{2\pi\alpha_0}\right)} - \frac{\xi\pi}{\lambda a}\sin\psi + \frac{\eta\pi}{2\alpha_0\lambda a}\sin^2\psi\right]\right\} \tag{29}$$

being the equivalent monostatic SAR transfer function (i.e., the receiver independent part of the FF-SAR transfer function)

$$H_n(\xi,\eta) \cong \exp\left(j\xi\Delta\bar{x}_{0n}\right)\exp\left[-j\eta\frac{\Delta r_{0n}}{\alpha_0}\right] \cdot w\left[\frac{\xi - \frac{2\pi}{\lambda}\sin\psi_0 + 2a_0\Delta\bar{x}_{0n}}{2aX_T}\right]\operatorname{rect}\left[\frac{\eta-\eta_{0n}}{2\pi\alpha_0\Delta f/c}\right] \tag{30}$$

is the bistatic, receiver dependent part of the FF-SAR transfer function, which also accounts for the effects of relative range offset [24] via the second exponential (while the differential range curvature [24] is ignored due to the approximation in (4): this is certainly acceptable with our assumptions on system parameters, see also [24])

$$a = \frac{\pi\beta}{\lambda r} \tag{31}$$

$$\Delta r_{0n} = \Delta r_{cn}(r_0,\vartheta_0) + \Delta r_{an}(r_0) \tag{32}$$

and $\Delta\bar{x}_{0n}$, α_0, a_0, and ψ_0 are the values of $\Delta\bar{x}_n$, α, a, and ψ evaluated at $r = r_0$.

Equation (30) shows that the azimuth bandwidth of the signals at all receivers is $\mathrm{BW_{az}} = 2\ aX_T = 2\pi\beta X_T/(\lambda r) = 2\pi\beta/L$, where L is the equivalent azimuth length of the real antenna so that the azimuth resolution is $L/\beta \cong L/2$,

i.e., approximately equal to (but slightly worse than, since $\beta < 2$) the monostatic SAR one. Similarly, the range bandwidth of the signals at all receivers is $2\pi\alpha_0\Delta f/c$, so that the slant range resolution is $c/(\alpha_0\Delta f) \cong c/(2\Delta f)$, i.e., approximately equal to (but slightly better than, since $\alpha_0 > 2$) the monostatic SAR one. However, (30) also shows that central frequencies of the signals at different receivers are mutually shifted both in azimuth, by $2a_0\Delta\bar{x}_{0n}$, and in range, by η_{0n}. In Section III, we will see that maximum SNR increase and ambiguity reduction can only be achieved if the azimuth shifts are negligible, i.e., if they are very small compared to the azimuth bandwidth so that the common bandwidth $2a_0(X_T - \Delta\bar{x}_N) \cong 2a_0(X_T - \Delta x_N/2) = 2a_0(X_T - l_R/4)$ is maximum. This implies that we must have $l_R/4 \ll X_T$. With this condition, and if b_R satisfies the condition mentioned in Section II-A, it is easy to verify, by using (16), (19), and (25), that η_{0n} is much smaller than the range bandwidth, so that the range central frequency shift can be neglected, too. Note that if mutual central frequency shifts can be neglected, the factors w and rect in (30) do not depend on n so that they can be moved from $H_n(\xi, \eta)$ to $G(\xi, \eta; r)$.

Finally, we note that if the desired range swath S_{WT} is too large to satisfy (20) and/or (21), then it must be subdivided into two or more smaller parts, each one satisfying (20) and (21), that must be separately processed.

Up to now, we have considered x' as a continuous variable, but actually, the signal in (22) and (23) is sampled with respect to x' at angular spatial frequency $\xi_s = 2\pi\text{PRF}/v$. Therefore, the actual FT $\tilde{S}'_n$ of (23) is the superposition of replicas of (27), spaced by ξ_s. If $\xi_s \geq 2\, aX_T/M$, i.e., the PRF is greater than $1/M$ the Doppler bandwidth $\beta v/L$, then only M replicas are nonnegligible, so that

$$\tilde{S}'_n(\xi, \eta) = \sum_{m=1}^{M} S'_n\left(\xi - m'\xi_s, \eta\right) = \sum_{m=1}^{M} H_{nm}(\xi, \eta) D_m(\xi, \eta) \tag{33}$$

where $-\xi_s/2 \leq \xi - \xi_{DC} \leq \xi_s/2$, $m' = m - \frac{M+1}{2}$ for M odd, or $0 \leq \xi - \xi_{DC} \leq \xi_s$, $m' = m - \frac{M}{2}$ for M even,

$$\xi_{DC} = \tfrac{2\pi}{\lambda} \sin\psi_0 \tag{34}$$

$$H_{nm}(\xi, \eta) = H_n\left(\xi - m'\xi_s, \eta\right)$$

$$D_m(\xi, \eta) = D\left(\xi - m'\xi_s, \eta\right). \tag{35}$$

Equation (33) can be expressed in matrix form as

$$\underline{\tilde{S}}'(\xi, \eta) = \underline{\underline{H}}(\xi, \eta)\underline{D}(\xi, \eta) \tag{36}$$

where $\underline{\tilde{S}}'(\xi, \eta)$ is an N-element column vector, $\underline{D}(\xi, \eta)$ is an M-element column vector, and $\underline{\underline{H}}(\xi, \eta)$ is an N-row-by-M-column matrix. Note that the matrix equation (36) is formally identical to the expression available in [16], [17], [18], and [19], but the analytical expressions of the involved matrix and vector elements are new.

III. Processing Algorithm

The signal model described in Section II leads to a three-step processing procedure: in the first step, an estimate $\hat{s}'_n$ of s'_n is obtained from the noisy range-compressed raw signals $\hat{s}_n$ by inverting (22); in the second step, an estimate $\hat{D}$ of the FT D of the equivalent monostatic raw signal is obtained from the FT $\hat{s}'_n$ of $\hat{s}'_n$ by inverting (36); and finally, in the third step, the final SAR image $\hat{\gamma}$ is obtained from $\hat{D}$ by using one of the available monostatic SAR processing techniques. The overall processing procedure is described in the block scheme of Fig. 4.

A. First Step: Baseline Phase Terms Compensation

The first processing step performs an accurate space-domain compensation of the cross-track and along-track baseline phase terms. Starting from the noisy range-compressed raw signals $\hat{s}_n$ and by inverting (22), we get

$$\hat{s}'_n\left(x', r'\right) = \exp\left\{ j\frac{2\pi}{\lambda}\left[\Delta r_{cn}\left(x', r'\right) + \Delta r_{an}\left(r'\right)\right]\right\}\hat{s}_n\left(x', r'\right). \tag{37}$$

This complex multiplication must be performed for the $N_a \times N_r$ pixels of the N raw signals. This processing step requires knowledge of the relative positions of the receivers with a centimetric precision, which is feasible. In addition, it requires knowledge of the scene height profile; however, if conditions on b_R mentioned in Section II-A are satisfied, a scene height accuracy of the order of several tens of meters is sufficient. Accordingly, this step is of paramount importance, but it does not present critical limitations.

B. Second Step: Combination of Receivers' Signals

The second processing step performs a proper combination of signals at different receivers, to remove azimuth ambiguity and to increase SNR. It is similar to the combination strategies available in [16], [17], [18], and [19], but, as already noted, the analytical expressions of involved matrix and vector elements are new.

First of all, 2-D FTs of $\hat{s}'_n$ are performed by using fast Fourier transform (FFT) algorithms, so obtaining $\hat{\tilde{S}}'_n$. From the latter, assuming $N \geq M$, estimates $\hat{D}_m$ of D_m are obtained by solving the matrix equation (36) in the least-squares sense

$$\underline{\hat{D}}(\xi, \eta) = \underline{\underline{H}}^{\dagger}(\xi, \eta)\underline{\hat{\tilde{S}}}'(\xi, \eta) \tag{38}$$

where $\underline{\underline{H}}^{\dagger} = \left(\underline{\underline{H}}^{*}\underline{\underline{H}}\right)^{-1}\underline{\underline{H}}^{*}$ is the pseudo inverse of $\underline{\underline{H}}$, and $\underline{\underline{H}}^{*}$ is its transpose conjugate. The unfolded unambiguous spectrum $\hat{D}(\xi, \eta)$ is then reconstructed by disposing the elements of the vector $\underline{\hat{D}}(\xi, \eta)$ over the ξ-axis, with $-M\xi_s/2 \leq \xi - \xi_{DC} \leq M\xi_s/2$, as illustrated in Fig. 5.

The performance of the reconstruction algorithm of (38) is measured by the (real nonnegative) eigenvalues λ_m of the $M \times M$ Hermitian square matrix $\underline{A} = \underline{\underline{H}}^{*}\underline{\underline{H}}$, whose elements are

$$A_{mp}(\xi, \eta) = \sum_{n=1}^{N} \exp\left[j(p - m)\xi_s\Delta\bar{x}_{0n}\right] w^{*}\left[\frac{\xi - \xi_{DC} - m'\xi_s + 2a_0\Delta\bar{x}_{0n}}{2aX_T}\right]$$

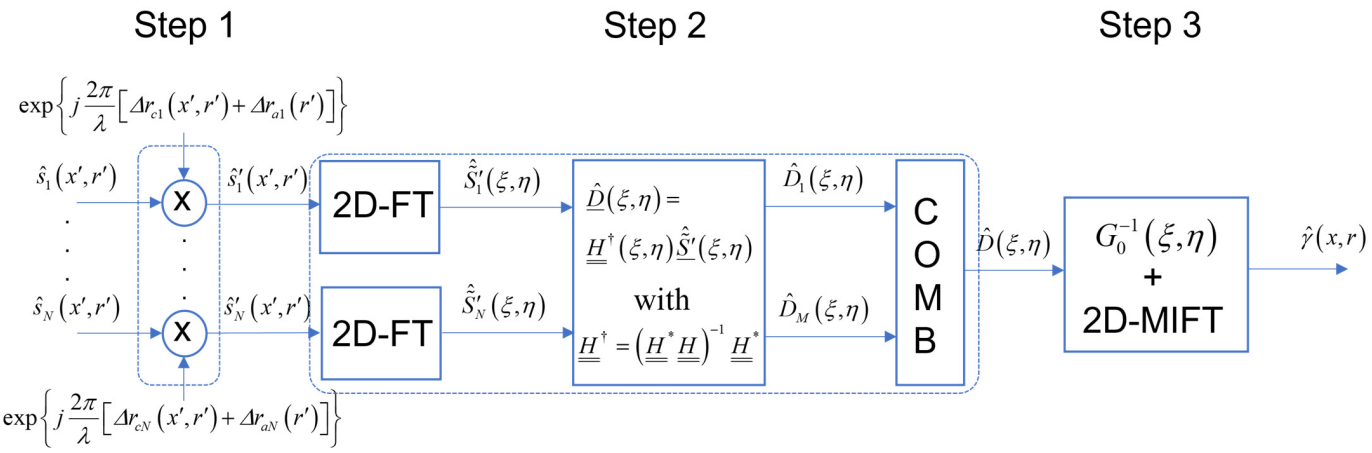

Fig. 4. Block scheme of the proposed FfT-FF-SAR processing chain. COMB stands for combination and MIFT stands for modified inverse FT, see (47).

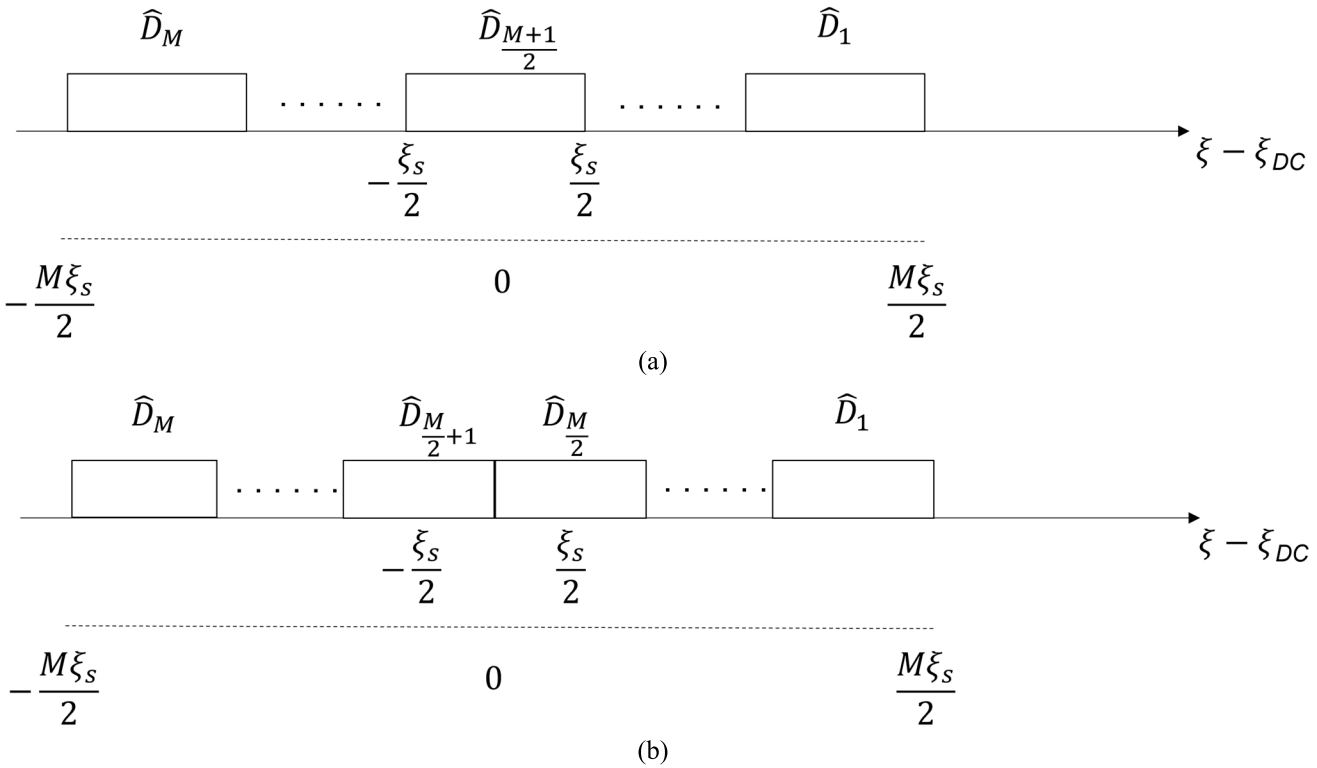

Fig. 5. Azimuth spectra reconstruction for: (a) M odd and (b) M even.

$$\cdot\, w\left[\frac{\xi-\xi_{DC}-p'\xi_s+2a_0\Delta\bar{x}_{0n}}{2aX_T}\right],\ \text{with } m,\, p=1,\ldots,M. \tag{39}$$

In fact, a measure of matrix conditioning, and thus of the ambiguity reduction, is provided by the condition number χ, which is the ratio of maximum to minimum eigenvalues. In addition, it can be shown [19] that the SNR after the signal combination is improved with respect to the SNR at the individual receivers by a factor G (SNR gain) given by

$$G=\frac{M}{\mathrm{Tr}\{\underline{\underline{A}}^{-1}\}}=\frac{M}{\sum_{m=1}^{M}\frac{1}{\lambda_m}}\le\frac{\sum_{m=1}^{M}\lambda_m}{M}=\frac{\mathrm{Tr}\{\underline{\underline{A}}\}}{M} \tag{40}$$

where $\mathrm{Tr}\{\underline{\underline{A}}\}$ stands for the trace of matrix $\underline{\underline{A}}$, and the Schwartz inequality has been applied to the vectors of components $(1/\lambda_m)^{1/2}$ and $(\lambda_m)^{1/2}$.

The ideal condition, which corresponds to maximum ambiguity suppression and SNR gain, is obtained when all the M eigenvalues coincide, i.e., when the matrix $\underline{\underline{A}}=\underline{\underline{H}}^{*}\underline{\underline{H}}$ is proportional to the identity matrix. In fact, in this case, $\chi=1$ and G attains the maximum value allowed by (40). This is achieved if the summation in (39) vanishes for $m\neq p$ and it is independent of m for $m=p$, i.e., if the following two conditions apply:

1) The formation length satisfies $l_R/4 \ll X_T$, so that, as noted in Section II-B, the mutual azimuth spectral

shift $2a_0\Delta\bar{x}_{0n}$ is negligible, w does not depend on n, and it can be moved from $H_n(\xi,\eta)$ to $G(\xi,\eta;r)$.

2) The receivers' positions are such that

$$\xi_s\left(\Delta\bar{x}_{0n}-\Delta\bar{x}_{01}\right)=2\pi\left(\frac{n-1}{N}+k_n\right),\ \text{i.e.,}$$
$$\Delta x_n-\Delta x_1=\frac{1+\cos^3\psi_0}{\cos^3\psi_0}\frac{v}{PRF}\left(\frac{n-1}{N}+k_n\right) \quad (41)$$

with integer k_n, so that for $m\neq p$, we get $A_{mp}=0$.

Condition 1) can be easily obtained since, for a typical X-band FF-SAR system, it corresponds to maximum formation lengths of the order of 500–1000 m. This condition is also very convenient from a computational viewpoint because it leads to a matrix $\underline{\underline{A}}$ independent of spatial frequencies ξ and η, so that matrix inversion must be performed only once

$$A_{mp}=\sum_{n=1}^{N}\exp\left[j(p-m)\xi_s\Delta\bar{x}_{0n}\right],\ \text{with } m,p=1,\ldots,M. \quad (42)$$

Therefore, from now on, we will assume that it is satisfied. In this case, $\mathrm{Tr}\{\underline{\underline{A}}\}=MN$, so that, in view of (40), the maximum attainable value of G is N.

Conversely, condition 2) cannot be easily obtained since it requires that the receiver platform orbits are controlled with a precision of the order of a small fraction of the SAR resolution, i.e., of the order of a few tens of centimeters. Actually, as noted in [16], [25], and [26], uncertainty on the relative sensor orbit control is much larger than that, being of the order of several meters. Accordingly, there is a nonnegligible probability that an ill-conditioned $\underline{\underline{A}}$ matrix, and hence significant ambiguity and reduced SNR, are obtained. Therefore, in Section IV, a complete statistical analysis of the performance of the reconstruction algorithm will be performed, by modeling Δx_n as a random variable and $\underline{\underline{A}}=\underline{\underline{H}}^*\underline{\underline{H}}$ as a stochastic matrix.

C. Third Step: Monostatic SAR Processing

The final unambiguous SAR image $\hat{\gamma}(x,r)$ is obtained from $\hat{D}(\xi,\eta)$ by resorting to usual monostatic SAR processing, which performs range migration correction and azimuth compression. Any algorithm able to process squinted stripmap SAR data can be used. For instance, a 2-D Fourier domain approach can be used: by proceeding as in [1], and also considering that S_{WT} is limited by (20) and (21), we can express (28) as

$$D(\xi,\eta)\cong\Gamma[\xi,\eta-\mu(\xi,\eta)]G_0(\xi,\eta) \quad (43)$$

where $G_0(\xi,\eta)=G(\xi,\eta;r_0)$ and

$$\mu(\xi,\eta)=\frac{\partial}{\partial r}\Phi(\xi,\eta;r)\bigg|_{r=r_0}\cong\frac{\xi^2}{4a_0r_0}=\mu(\xi) \quad (44)$$

with

$$\Phi(\xi,\eta;r)=\frac{\xi^2}{4a\left(1+\frac{\eta\lambda}{2\pi\alpha}\right)}-\frac{\xi\pi}{\lambda a}\sin\psi+\frac{\eta\pi}{2\alpha\lambda a}\sin^2\psi. \quad (45)$$

Therefore, from $\hat{D}(\xi,\eta)$, we can obtain the (shifted) FT of the final SAR image as

$$\hat{\Gamma}[\xi,\eta-\mu(\xi)]=\hat{D}(\xi,\eta)G_0^{-1}(\xi,\eta) \quad (46)$$

and the final SAR image as

$$\hat{\gamma}(x,\bar{r})=FT_x^{-1}\left\{\exp\left[-j\mu(\xi)\bar{r}\right]FT_r^{-1}\left\{\hat{\Gamma}[\xi,\eta-\mu(\xi)]\right\}\right\} \quad (47)$$

where FT_x^{-1} and FT_r^{-1} are the azimuth and range inverse FTs, respectively, and $\bar{r}=r-r_0$.

Finally, we note that in the case $M=1$, the whole above-described procedure reduces to simply rephasing and coherently summing up the N individual complex SAR images, thus leading to an SNR gain ideally equal to N.

IV. Performance Analysis

As noted in Section III-B, the performance of the reconstruction algorithm of (38) is governed by the eigenvalues λ_m of the matrix $\underline{\underline{A}}$. By assuming that this matrix can be expressed by (42), its eigenvalues, and thus condition number and SNR gain, depend on the products $\phi_n=\xi_s\Delta\bar{x}_{0n}$, i.e., for a fixed d, on the PRF and on the receivers' relative positions Δx_n. If ϕ_n is varied by spanning an interval wider than 2π (which is obtained by varying the receivers' positions by distances of the order of SAR resolution, i.e., of the order of the physical size of the transmitting antenna), then the entire range of possible values of condition number and SNR gain is obtained. Since the uncertainty on the relative sensor positions control is usually of the order of several meters, there is a nonnegligible probability that an ill-conditioned

A matrix, and thus significant ambiguity and reduced SNR, is obtained.

In this section, we first of all highlight the relation between SNR gain and condition number. Then, by modeling the receivers' positions as random variables, we perform a statistical analysis of SNR gain and condition number, both assuming a fixed PRF and allowing for an adaptive PRF tuning. Finally, we numerically verify the overall proposed processing algorithm by applying it to simulated raw signals.

A. Relation Between SNR Gain and Condition Number

Let us order the eigenvalues λ_m in the ascending order, so that

$0\leq\lambda_m\leq\lambda_{m+1}\leq\lambda_M$ for $m=1,\ldots,M-1$. Accordingly, the condition number is

$$\chi=\frac{\lambda_M}{\lambda_1}. \quad (48)$$

We also have

$$\sum_{m=1}^{M}\lambda_m=\lambda_1\sum_{m=1}^{M}a_m=\mathrm{Tr}\left\{\underline{\underline{A}}\right\}=MN\Rightarrow\lambda_1=\frac{MN}{\sum_{m=1}^{M}a_m} \quad (49)$$

where $a_m=\lambda_m/\lambda_1$, so that $a_1=1$, $a_M=\chi$, and if $M>2$, $1\leq a_m\leq a_{m+1}\leq\chi$ for $m=2,\ldots,M-1$.

By using (49) in (40), we obtain the following expression of the SNR gain:

$$G=\frac{M}{\sum_{m=1}^{M}\frac{1}{\lambda_m}}=\frac{M\lambda_1}{\sum_{m=1}^{M}\frac{1}{a_m}}=\frac{M^2N}{\sum_{m=1}^{M}\frac{1}{a_m}\sum_{m=1}^{M}a_m}$$

$$= N\frac{M^2}{\left(1+\sum_{m=2}^{M-1}\frac{1}{a_m}+\frac{1}{\chi}\right)\left(1+\sum_{m=2}^{M-1}a_m+\chi\right)}$$
$$= N\frac{M^2\chi}{\left(1+\chi\sum_{m=2}^{M-1}\frac{1}{a_m}+\chi\right)\left(1+\sum_{m=2}^{M-1}a_m+\chi\right)}. \quad (50)$$

For $M = 2$, we get

$$G = N\frac{4\chi}{(1+\chi)^2} \quad (51)$$

which shows that in this case, a one-to-one correspondence exists between SNR gain and condition number [see Fig. 6(a)]. This is not the case for $M > 2$ because G also depends on the values of a_m. However, G and χ are still strictly related, especially for small values of M since, for each value of χ, G is limited to a range of values that becomes narrower as M is decreased. This can be seen by considering G, for a fixed χ, as a function of the variables $a_2, \ldots, a_{M-1}$. As we show in Appendix C, the maximum value of this function is

$$G_{\max} = N\frac{M^2\chi}{\left[1+(M-2)\sqrt{\chi}+\chi\right]^2} \quad (52)$$

and its minimum value is

$$\begin{cases} G_{\min} = N\dfrac{4\chi}{(1+\chi)^2} & \text{for } M \text{ even} \\ G_{\min} = N\dfrac{4\chi}{(1+\chi)^2-\frac{1}{M^2}(\chi-1)^2} & \text{for } M \text{ odd.} \end{cases} \quad (53)$$

Note that (52) and (53) reduce to (51) for $M = 2$, and that for large M, the second of (53) is approximately equal to the first.

Plots of the relation between SNR gain and condition number for M values from 2 to 5 are shown in Fig. 6.

Finally, we explicitly note that the original results of this section apply to both the conventional and the FfT configurations of FF-SAR.

B. Statistical Analysis of SNR Gain and Condition Number

Let us first suppose that the transmitter PRF cannot be varied. This is the case, for instance, if an SAR transmitter of opportunity is employed. Since the uncertainty on the control of receiver positions is of the order of several meters, the phases $\phi_n = \xi_s \Delta\bar{x}_{0n}$ can be modeled as independent random variables uniformly distributed in $[-\pi, \pi]$. Accordingly, the matrix $\underline{\underline{A}}$ in (42) is a random matrix, to which theoretical results of [27] can be applied. As noted in [16], these results imply that a condition number smaller than 10 (and thus a sufficiently well-conditioned matrix) is obtained for N equal to at least $3M$. It is interesting to note that by letting $\chi = 10$ and $N = 3M$ in (53), we get that the SNR gain is equal to at least M, i.e., at least the value obtained for $N = M$ in the ideal conditions of (41). However, it must be noted that theoretical results of [27] hold for large matrices (more exactly, for $M \to \infty$). Conversely, in the present application, M is usually small. Therefore, we here want to explore the statistics of condition number χ and SNR gain G for small values of M. To this aim, by using Monte Carlo simulations, we have computed the cumulative distribution function (cdf) of χ and G for $M = 2, 3, 4$ and for different values of N. These cdfs are plotted in Fig. 7. From these graphs, for each M, we can evaluate the minimum number of receivers N such that $\chi < 10$ with a probability greater than 0.95 and, similarly, the minimum number of receivers N such that $G > M$ with probability greater than 0.95. For $M = 2$, both aims are achieved for $N = 5$, and for $M = 3$, both aims are achieved for $N = 9 = 3M$. For $M = 4$, the minimum number of receivers such that $G > M$ with a probability greater than 0.95 is $N = 12 = 3M$, whereas a larger number of receivers would be needed if we require that $\chi < 10$ with a probability greater than 0.95. However, for $N = 12$, the probability that $\chi < 10$ is about 0.9, which may be still acceptable.

TABLE I

PROBABILITY THAT $\chi < 10$ (OR $G > M$) WHEN THE PRF IS TUNED IN AN INTERVAL OF $\pm 3\%$ AROUND ITS NOMINAL VALUE

Number of receivers N	*M=2*		*M=3*		*M=4*	
	χ<10	*(G>M)*	*χ<10*	*(G>M)*	*χ<10*	*(G>M)*
2	1.000	(0)	-		-	
3	1.000	(1.000)	0.704	(0)	-	
4	1.000	(1.000)	0.975	(0.779)	0.559	(0)
5	1.000	(1.000)	0.998	(0.985)	0.740	(0.352)
6	1.000	(1.000)	1.000	(0.999)	0.927	(0.798)
7	1.000	(1.000)	1.000	(1.000)	0.988	(0.974)
8	1.000	(1.000)	1.000	(1.000)	0.999	(0.999)

In conclusion, we can state that for $M = 2$, a proper choice is $N = 5$, whereas for $M > 2$, we should choose $N = 3M$.

Let us now move to the case in which PRF tuning can be performed, as proposed in the literature [16], [25]: for given receiver positions Δx_n, the PRF can be adaptively modified within a prescribed interval in order to minimize the condition number χ. In particular, we assume that the PRF can be varied in an interval of $\pm 3\%$ around its nominal value PRF_0, i.e., between $\mathrm{PRF}_0 - 0.03\mathrm{PRF}_0$ and $\mathrm{PRF}_0 + 0.03\mathrm{PRF}_0$. In addition, we assume that $\Delta\bar{x}_{0n} - \Delta\bar{x}_{01}$ are Gaussian random variables with a mean equal to $(n-1)50$ m and a standard deviation equal to 2.5 m. This means that $\Delta x_n - \Delta x_1$ are Gaussian random variables with a mean equal to about $(n-1)100$ m and standard deviation equal to about 5 m, the exact values depending on ψ_0. In addition, we assume that the nominal value of ξ_s is $2\pi/(3M)$ m^{-1}, which corresponds to a SAR system with azimuth resolution $L/2$ not larger than 3 m. By performing Monte Carlo simulations, we have evaluated the probability that $\chi < 10$ and that $G > M$ for $M = 2, 3, 4$ and for different values of N. Results are reported in Table I. It turns out that for $M = 2$, the condition number is always smaller than 10 for any N, including $N = 2$. From Table I, we note that the minimum number of receivers N such that $\chi < 10$ with a probability greater than 0.95 is $N = 4$ for $M = 3$ and $N = 7$ for $M = 4$; for $M = 3$, N must be increased by one if we require that $G > M$ with probability greater than 0.95. We have verified that practically the same results are obtained if the PRF is adaptively modified to maximize G instead that to minimize χ.

Again, we explicitly note that these results are new not only for the FfT configuration, but also for the conventional FF-SAR, which is recovered by simply letting $\Delta\bar{x}_{0n} = \Delta x_n/2$.

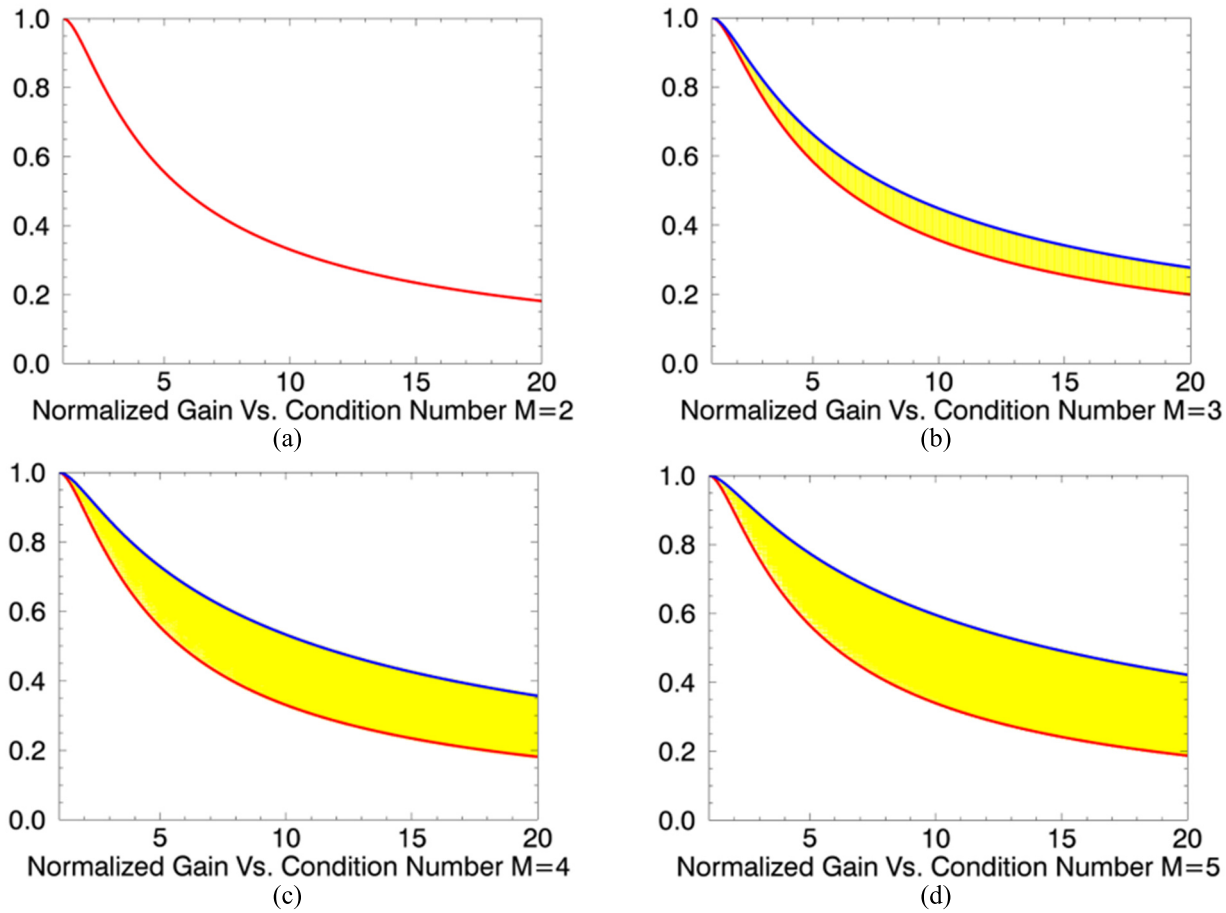

Fig. 6. Normalized gain G/N versus condition number χ for: (a) $M = 2$; (b) $M = 3$; (c) $M = 4$; and (d) $M = 5$. For $M > 2$, the yellow area between blue and red curves represents the allowed G–χ pairs.

TABLE II
FF-SAR SYSTEM PARAMETERS

Parameter	Value
Orbit altitude	410 km
Satellite velocity	7.7 km/s
Tx antenna length (azimuth)	3.4 m
Carrier wavelength	0.031 m
Monostatic nominal resolution	1.88 m × 1.70 m
Radar look-angle	30°
Number of satellites	5
PRF	5400 Hz (M=1) 2000 Hz (M=3)
Chirp bandwidth	80 MHz
Pulse duration	20 µs
Sampling frequency	96 MHz
SNR at the single Rx	30 dB

C. Processing Algorithm Verification

In this section, we report numerical results illustrating the output of the processing chain described in Section III applied to a point target located at the scene center, unless otherwise stated, in the case $M = 1$ (Section IV-C1) and $M > 1$ (Section IV-C2).

Simulation parameters are listed in Table II. In the whole simulation study, we assumed an FF-SAR working at 9.6 GHz (X-band) and comprising a formation of five satellites unless otherwise stated. The achieved range swath can be evaluated as

$$S_{\mathrm{r}} = \frac{c(\mathrm{PRI} - 2\tau)}{2\sin\vartheta} \tag{54}$$

where PRI is the pulse repetition interval, τ is the chirp pulse duration, and ϑ is the radar look-angle. For the FF-SAR defined in Table II, we obtain a range swath of about 43 km.

Output results are shown with an oversampling factor of 25 for visualization purposes.

Raw signals have been simulated assuming the parameter values reported in Table II and assuming the ideal geometry described in Section II, including straight flight paths, constant Tx and Rxs velocities, and constant d and Δx over time.

The aim of the simulation analysis is to provide quantitative and qualitative indications about the expected performance of the proposed processing algorithm.

The following imaging performance parameters have been considered:

- range and azimuth resolutions, evaluated as the 3-dB impulse response width (IRW) in intensity format;
- peak-to-sidelobe ratio (PSLR), defined as

$$\mathrm{PSLR}_{\mathrm{dB}} = 10\log_{10}\frac{\mathrm{SLL}}{\mathrm{MLL}} \tag{55}$$

where SLL and MLL stand for the sidelobe and mainlobe levels, respectively;

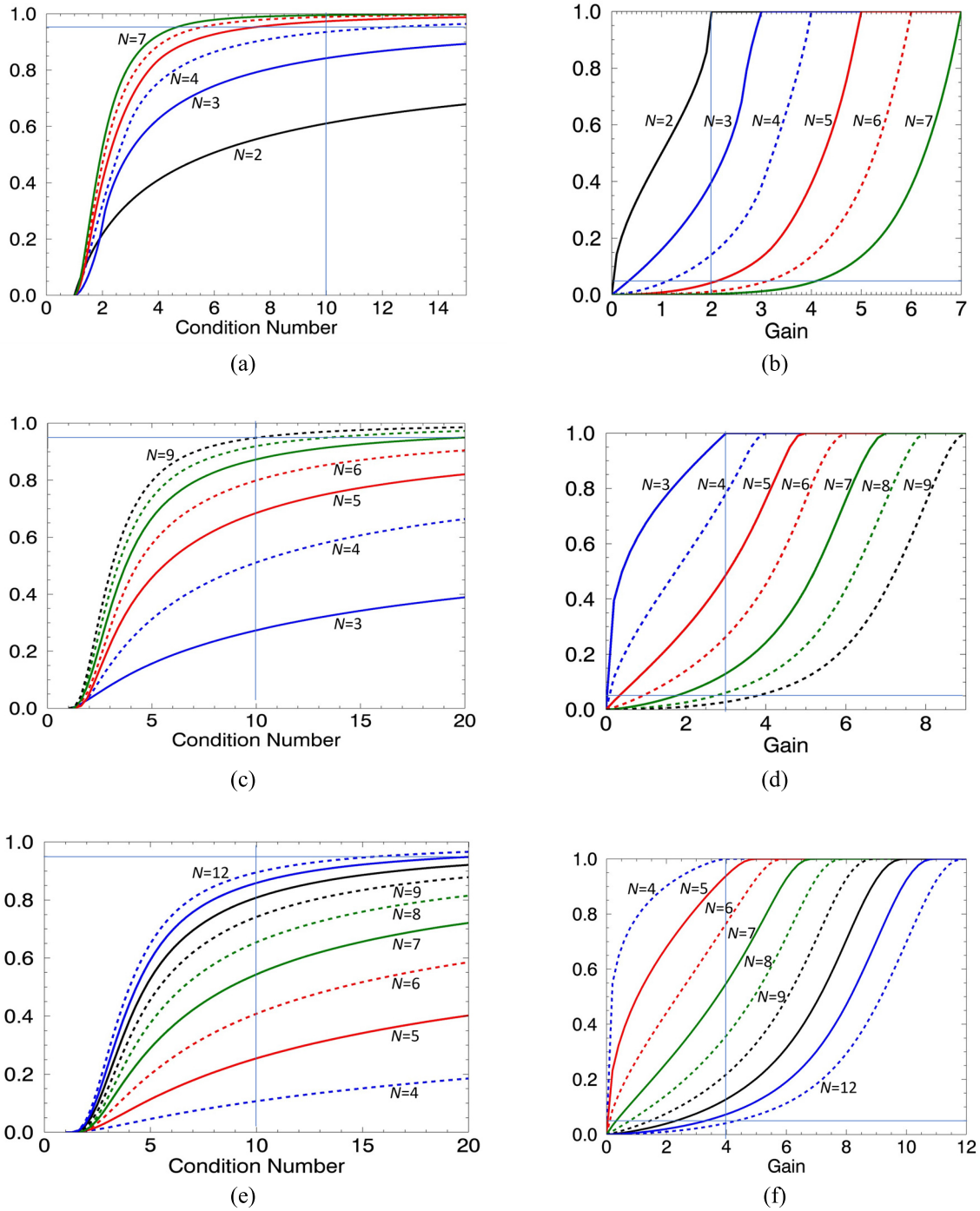

Fig. 7. cdfs of condition number and gain for: (a) and (b) $M = 2$; (c) and (d) $M = 3$; and (e) and (f) $M = 4$. Thin vertical and horizontal lines represent $\chi = 10$ and cdf $= 0.95$ in (a), (c), and (e), and $G = M$ and cdf $= 0.05$ in (b), (d), and (f).

- integrated sidelobe ratio (ISLR), defined as

$$\mathrm{ISLR_{dB}} = 10\log_{10}\frac{\mathrm{SL_{en}}}{\mathrm{ML_{en}}} \tag{56}$$

where

$$\mathrm{ML_{en}} = \iint_{\mathrm{ML}} \left|\hat{\gamma}\left(x', r'\right)\right|^2 \mathrm{d}x'\mathrm{d}r' \tag{57}$$

and

$$\mathrm{SL_{en}} = \iint_{(10\mathrm{d}x,\,10\mathrm{d}r)} \left|\hat{\gamma}\left(x', r'\right)\right|^2 \mathrm{d}x'\mathrm{d}r' - \mathrm{ML_{en}} \tag{58}$$

are the mainlobe and sidelobes energy levels, respectively; the integration domain of (57) covers the full area of the impulse response mainlobe; dx and dr stand for the azimuth and range IRWs, respectively. The integral domain approximately contains 98% of the overall sinc function energy;

- SNR gain, defined as

$$G = \frac{\mathrm{SNR}_N}{\mathrm{SNR}_1} \tag{59}$$

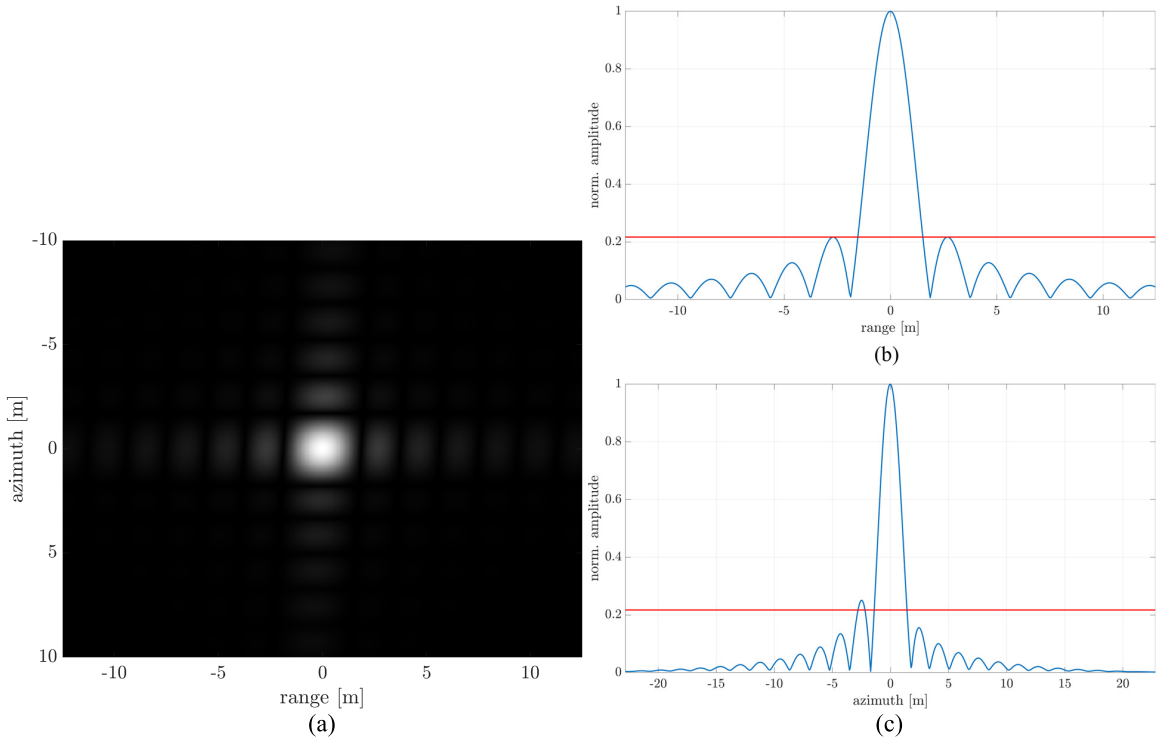

Fig. 8. (a) 2-D SAR image, and normalized: (b) range and (c) azimuth amplitude profiles for $M = 1$, $d = 50$ km, and $\Delta x = 100$ m. Remaining FF-SAR parameters are listed in Table II. An oversampling factor of 25 has been applied. The red lines indicate the sinc function SLL.

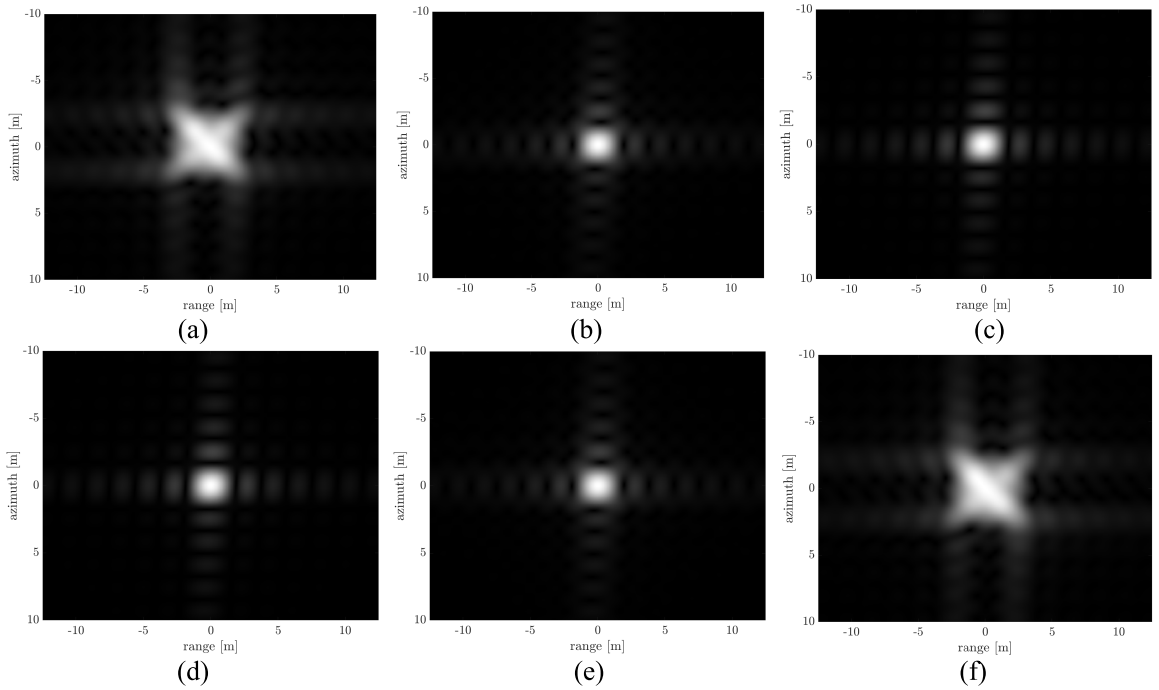

Fig. 9. 2-D impulse response for $M = 1$, $d = 50$ km, $\Delta x = 50$ m, and target ground range of: (a) -20 km; (b) -5 km; (c) -1 km; (d) 1 km; (e) 5 km; and (f) 20 km. In each configuration, the origin of the range axis has been set in correspondence of the target for visualization purposes.

where SNR_1 and SNR_N stand for the SNR at the receiver of the single satellite and of the whole N-sat formation.

Along with the abovementioned quality indicators, in the case $M > 1$, the azimuth ambiguity suppression capability is evaluated via the peak azimuth ambiguity-to-signal ratio (PAASR), which is defined as follows:

$$\mathrm{PAASR}_{\mathrm{dB}} = 10 \log_{10} \frac{P_{\mathrm{aa}}}{P_{\mathrm{s}}} \tag{60}$$

where P_{aa} and P_{s} stand for the largest azimuth ambiguity level and the target mainlobe peak, in intensity format.

Geometric and radiometric parameters, namely, PSLR, ISLR, and spatial resolutions have been evaluated in noise-free conditions to provide more accurate analyses. For fair SNR gain evaluation, a signal bandwidth of ξ_{s} is processed for the single satellite case; additionally, reported results have been obtained by averaging ten independent runs.

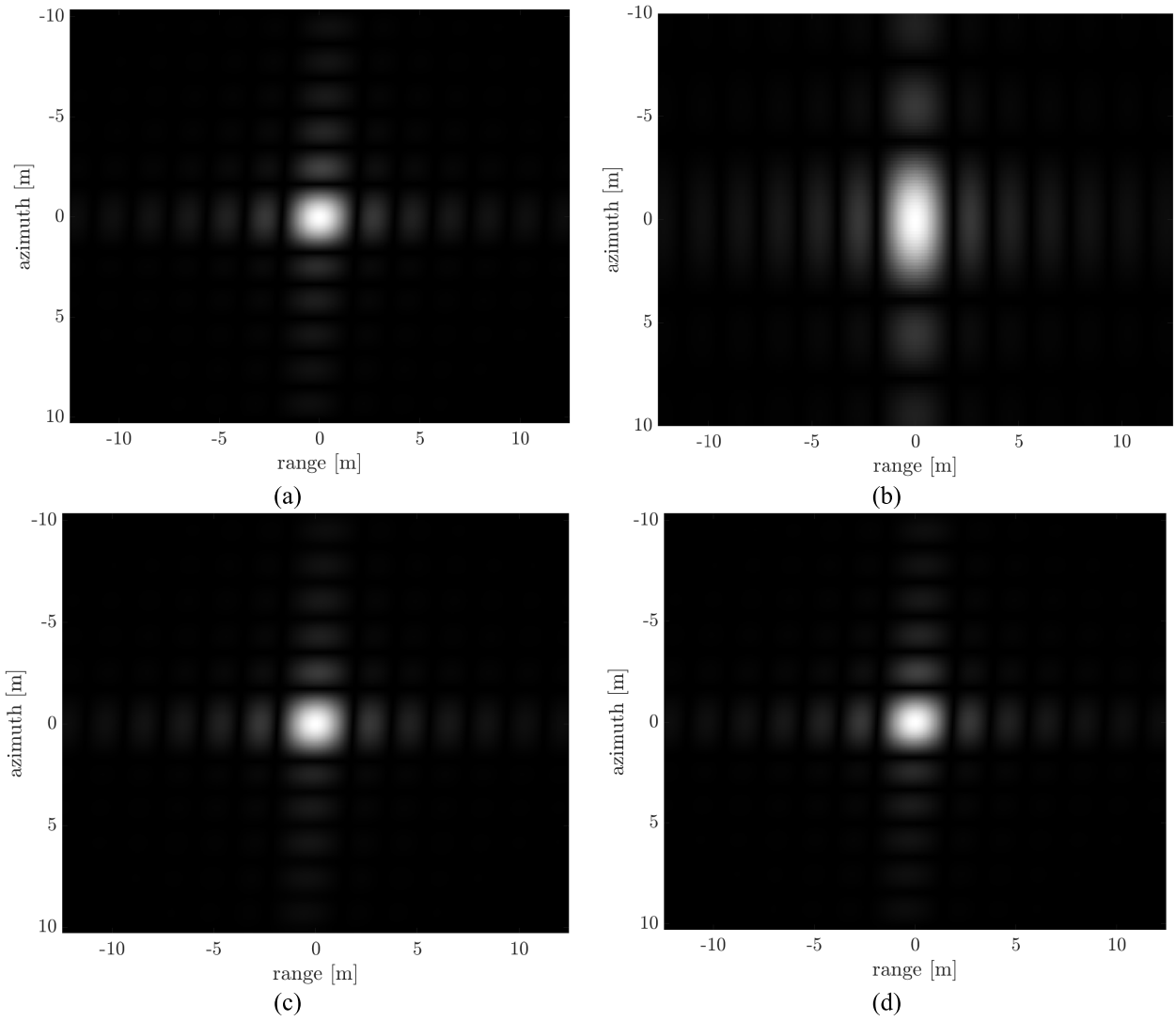

Fig. 10. 2-D impulse response of target for $M = 3$ (PRF = 2000 Hz), $d = 50$ km, and: (a) Δx ideal, $N = 3$; (b) $N = 1$; (c) $\Delta x = 50$ m, $N = 3$; and (d) $\Delta x = 50$ m, $N = 9$.

In Figs. 8–12, the range axis has to be intended as a slant range.

1) Case $M = 1$: In this system configuration, the operating PRF is larger than the received signal bandwidth $\mathrm{BW_{az}}$; hence, no azimuth ambiguity raises in the final bistatic image. This acquisition mode is aimed at improving the SNR of the FF-SAR with respect to an equivalent monostatic SAR, i.e., a hypothetical backscattering SAR sensor mounted onboard the FF-SAR transmitter of opportunity. FF-SAR system parameters are listed in Table II. Imaging performance metrics relevant to a single point target located at the scene center are reported in Table III for different Tx–Rxs distance d and along-track baselines Δx. For the sake of conciseness, we only show the impulse response relevant to the case $d = 50$ km and $\Delta x = 100$ m in Fig. 8. Obtained radiometric and geometric performance indicators are in line with the ideal sinc impulse response, thus demonstrating the effectiveness of the data synthesis algorithm in aliasing-free conditions. In particular, the achieved spatial resolution is similar to the nominal values in Table II. The coherent combination of the received signals spectra leads to a significant increase of the final SNR with respect to the single receiver. Actually, the achieved SNR gain is very close to the maximum nominal value N for small Tx–Rxs distance and along-track baseline, while a slight degradation is measured as both distances increase, thus leading to a reduced noise rejection capability of the FF-SAR formation. Such a performance degradation might be partially motivated by the degraded compression and focusing capabilities of the data synthesis algorithm for large target-scene center offset.

Imaging capabilities are expected to be dependent upon the target ground-range position, due to the approximations made, namely, $r = r_0$ when moving to the Fourier domain. Accordingly, for a more comprehensive performance analysis, here, we evaluate imaging metrics for a single point target at different ground-range coordinates. The FF-SAR system parameters are listed in Table II. Additionally, we consider $d = 50$ km, $\Delta x = 50$ m, and $N = 5$. Synthetic results are reported in Table IV, while, for the sake of conciseness, only few cases are shown in Fig. 9. The ground range axis has the

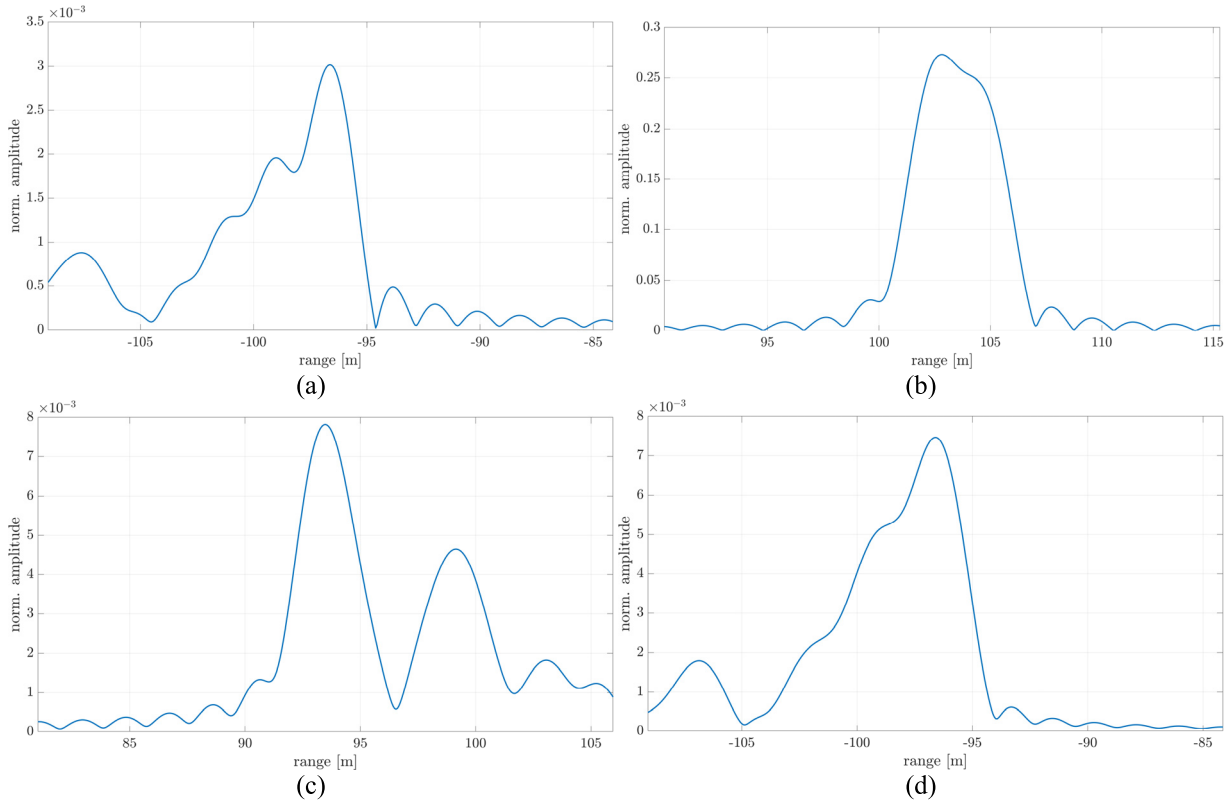

Fig. 11. Strongest ghost range profile for $M = 3$ (PRF = 2000 Hz), $d = 50$ km, and: (a) Δx ideal, $N = 3$; (b) $N = 1$; (c) $\Delta x = 50$ m, $N = 3$; and (d) $\Delta x = 50$ m, $N = 9$. Note that the vertical scales are different in different plots. Amplitudes are normalized to the target one.

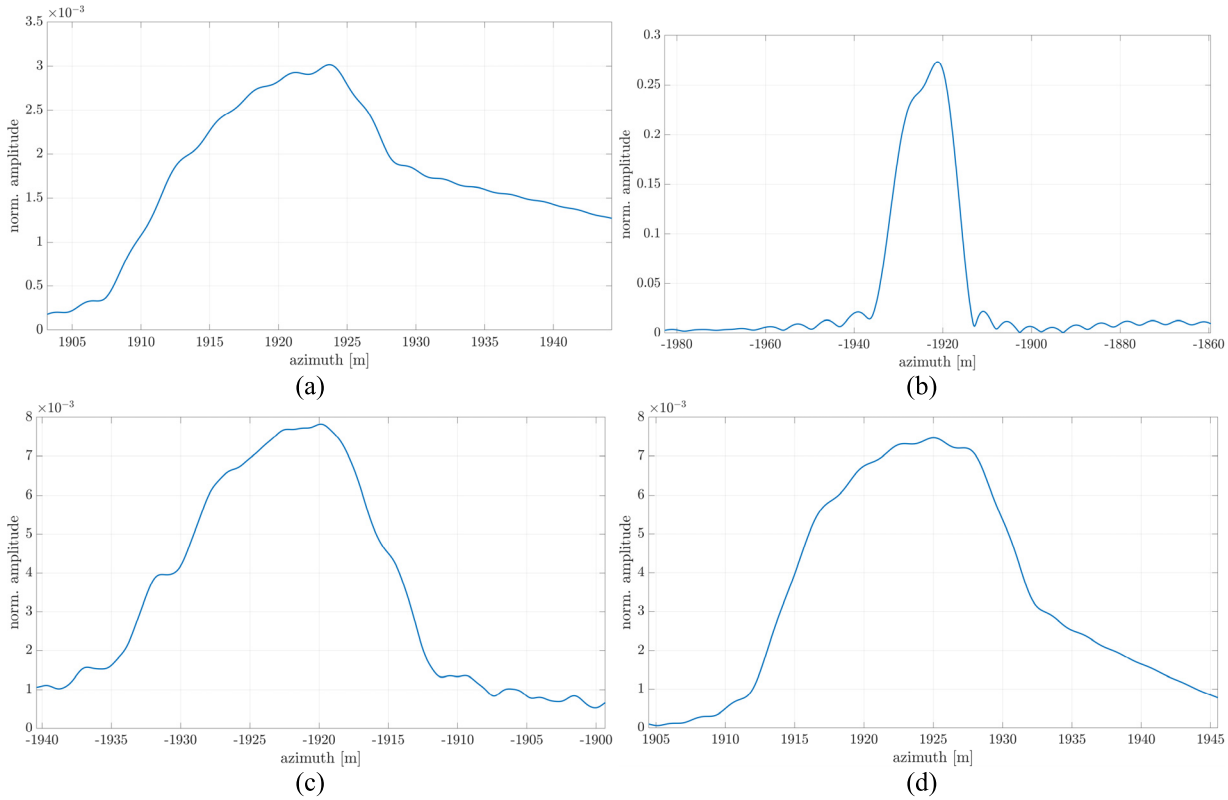

Fig. 12. Strongest ghost azimuth profile for $M = 3$ (PRF = 2000 Hz), $d = 50$ km, and: (a) Δx ideal, $N = 3$; (b) $N = 1$; (c) $\Delta x = 50$ m, $N = 3$; and (d) $\Delta x = 50$ m, $N = 9$. Note that the vertical scales are different in different plots. Amplitudes are normalized to the target one.

origin at the scene center and points from the Tx outward. Performance indicators are quite stable for absolute values of target ground ranges up to 10 km and significantly degrade for larger distances, where the impulse response severely deviates from the ideal pattern due to the approximations made, as it is also clear from Fig. 9. The SNR gain is largest at scene

TABLE III
IMAGING PERFORMANCE PARAMETERS FOR $M = 1$, $N = 5$, AND DIFFERENT FF-SAR CONFIGURATIONS

d (km)	Δx (m)	PSLR (dB)	ISLR (dB)	IRW range (m)	IRW azimuth (m)	G
20	50	-12.59	-7.73	1.62	1.48	5.0
20	100	-12.66	-7.84	1.62	1.43	5.0
50	50	-11.71	-7.70	1.62	1.48	4.9
50	100	-11.95	-7.92	1.62	1.48	4.7

TABLE IV
IMAGING PERFORMANCE PARAMETERS FOR $M = 1$, $N = 5$, AND DIFFERENT TARGET GROUND-RANGE POSITIONS

Target ground-range (km)	PSLR (dB)	ISLR (dB)	IRW range (m)	IRW azimuth (m)	G
-20	-10.71	-9.69	3.05	2.85	1.0
-10	-11.23	-8.02	1.81	1.65	3.1
-5	-12.43	-7.70	1.62	1.48	4.3
-3	-11.94	-7.73	1.62	1.43	4.7
-1	-11.72	-7.70	1.62	1.48	4.8
-0.5	-11.70	-7.70	1.62	1.48	4.9
-0.1	-11.70	-7.70	1.62	1.48	4.9
0.1	-11.71	-7.70	1.62	1.48	4.9
0.5	-11.72	-7.70	1.62	1.48	4.8
1	-11.76	-7.70	1.62	1.48	4.9
3	-12.04	-7.72	1.62	1.48	4.6
5	-12.60	-7.72	1.68	1.48	4.4
10	-11.78	-8.04	1.75	1.65	3.1
20	-10.53	-10.12	2.99	2.97	1.1

TABLE V
IMAGING PERFORMANCE PARAMETERS FOR $M = 3$

Δx (m)	N	PSLR (dB)	ISLR (dB)	IRW range (m)	IRW az. (m)	PAASR (dB)	G
ideal	3	-11.63	-7.62	1.62	1.49	-50.41	3.0
-	1	-13.13	-7.78	1.56	3.23	-11.27	1.0
50	3	-12.82	-8.31	1.62	1.49	-42.13	1.1
50	9	-11.79	-7.80	1.62	1.49	-42.54	8.8

center and gradually degrades as the target moves away. For targets located at 20 km from the scene center, or farther, the receivers' formation is no longer effective in rejecting thermal noise with respect to the single receiver.

2) Case $M > 1$: In this acquisition mode, the transmitter sends chirp pulses at a PRF below the Nyquist limit in order to enlarge significantly the range swath. By recombining the received signals as described in Section III, the unambiguous azimuth spectrum can be reconstructed and the resulting ambiguities in the azimuth direction due to the reduced PRF are attenuated to some extent depending on the number of receivers and M.

In this simulation setup, we assumed PRF $= 2000$ Hz, which for an azimuth bandwidth of about 4500 Hz leads to $M = 3$. Additionally, the distance d between the Tx and the Rxs formation center is set to 50 km for all the cases analyzed. The remaining system parameters are those listed in Table II. To provide a more accurate performance evaluation, thermal noise has been injected in raw data only for the evaluation of the SNR gain. Imaging quality indicators are shown in Table V for different along-track baselines Δx and the number of receiving platforms N. The 2-D images of the target are shown in Fig. 10, while range and azimuth normalized profiles of the strongest ghost due to azimuth ambiguity are shown in Figs. 11 and 12, respectively. An ideal case where Rxs positions have been set according to (41) has also been considered. Such a configuration provides the best azimuth ambiguities suppression for a fixed M. For the FF-SAR analyzed here, (41) results in an along-track baseline of about 18.12 m. In the nonideal case of $\Delta x = 50$ m, the azimuth ambiguity suppression capability improves with increasing N, but it remains well below the ideal formation case, even for a number of satellites significantly larger than M. As for thermal noise suppression, it is worth noting that the ideal configuration with M satellites ensures the best possible noise reduction, i.e., an SNR gain approximately equal to N. Conversely, a nonideal formation provides less predictable performance due to the different receivers' distances from the ideal ones. Notwithstanding, the case with $N = 9$ leads to a much larger SNR gain than the one with $N = 3$, which actually justifies the adoption of a larger formation despite the fact that azimuth ambiguity suppression capability no longer significantly improves. Finally, it is worth noting that configurations with $N < M$ do not represent meaningful FF-SAR operating conditions as M is the minimum number of receivers required to recover the whole azimuth spectrum.

V. CONCLUSION

We have presented an analytical model for the signal received by an FF-SAR, i.e., a multistatic distributed SAR based on a cluster of satellite receivers orbiting in coordinated motion and receiving the signal emitted from an SAR transmitter which is part of the cluster or opportunistically exploited. As opposed to conventional approaches, which assume that the transmitter-to-receiver baseline is much smaller than satellite altitude, in this article, we focus on FfT geometry, where this assumption does no longer hold. In this configuration, the FF-SAR transfer function is demonstrated to be composed of a receiver dependent part—accounting for received signal spectrum shift in both azimuth and range directions due to receivers' separation, along-track and cross-track baselines—and a receiver independent part, i.e., the equivalent monostatic SAR transfer function—accounting for range migration and azimuth defocusing of each received echo.

Additionally, we presented an efficient three-step processing scheme in the transform domain, stemming from the developed signal model, and based on a proper coherent combination and spectrum reconstruction of the received echoes. The proposed data synthesis approach is suited to two FF-SAR imaging modes, namely, SNR improvement—where the coherent processing is aimed at reducing noise power—and HRWS—where spectrum reconstruction attenuates azimuth ambiguities. Ideal FF-SAR configurations maximizing SNR gain and ambiguity suppression were also investigated and discussed. An original formulation of the relation between SNR gain and condition number has also been provided. In addition, by modeling the receivers' positions as random variables, a statistical analysis

of SNR gain and condition number has been carried out, both assuming a fixed PRF and allowing for an adaptive PRF tuning.

Simulation results show that radiometric and geometric imaging capabilities achieved by the proposed processing scheme are aligned with those offered by the equivalent monostatic SAR. For SNR improvement, noise suppression capability is strongest at the scene center and remains at acceptable levels for target-scene center offset up to several kilometers. Finally, in HRWS imaging mode, azimuth ambiguity suppression improves as the number of satellites increases but remains below that offered by ideal FF-SAR. Assessment of imaging performance in the presence of extended targets as well as a comprehensive analysis of the role of the receiver formation parameters on imaging capabilities might require proper attention and will be investigated in the near future.

APPENDIX A

In this appendix, we show how (6)–(11) are obtained.

From (3) and (4), we have

$$r_{\mathrm{T}}+r_n = r+\frac{\left(x'-x\right)^2}{2r}+\frac{r}{\cos\psi}-\sin\psi\left(x'-x+\Delta x_n\right) + \cos^3\psi\frac{\left(x'-x+\Delta x_n\right)^2}{2r}-\cos\psi b_n\cos(\theta_n-\theta). \tag{61}$$

Let us consider the following terms that appear in (61):

$$\cos^3\psi\frac{\left(x'-x+\Delta x_n\right)^2}{2r}+\frac{\left(x'-x\right)^2}{2r}. \tag{62}$$

By adding and subtracting $A\Delta x_n$, with A being an arbitrary constant, in the parentheses of (62), we get (63), as shown at the bottom of the next page, which can be rewritten as

$$\left(\cos^3\psi+1\right)\frac{\left(x'-x+A\Delta x_n\right)^2}{2r}+\left[\cos^3\psi(1-A)-A\right] \cdot\frac{2\left(x'-x+A\Delta x_n\right)\Delta x_n}{2r}+\left[(1-A)^2\cos^3\psi+A^2\right]\frac{\Delta x_n^2}{2r}. \tag{64}$$

We can now determine the constant A by imposing

$$\cos^3\psi(1-A)-A=0 \tag{65}$$

from which

$$A=\frac{\cos^3\psi}{1+\cos^3\psi}\ \text{and}\ (1-A)=\frac{1}{1+\cos^3\psi} \tag{66}$$

so that $A\Delta x_n=\Delta\bar{x}_n$.

By replacing (66) in (64), we get

$$\left(\cos^3\psi+1\right)\frac{\left(x'-x+\Delta\bar{x}_n\right)^2}{2r} + \left[\left(\frac{1}{1+\cos^3\psi}\right)^2\cos^3\psi+\left(\frac{\cos^3\psi}{1+\cos^3\psi}\right)^2\right]\frac{\Delta x_n^2}{2r} = \left(\cos^3\psi+1\right)\frac{\left(x'-x+\Delta\bar{x}_n\right)^2}{2r} + \left[\frac{\cos^3\psi}{\left(1+\cos^3\psi\right)^2}+\frac{\left(\cos^3\psi\right)^2}{\left(1+\cos^3\psi\right)^2}\right]\frac{\Delta x_n^2}{2r}. \tag{67}$$

In conclusion, we have

$$\cos^3\psi\frac{\left(x'-x+\Delta x_n\right)^2}{2r}+\frac{\left(x'-x\right)^2}{2r} = \left(\cos^3\psi+1\right)\frac{\left(x'-x+\Delta\bar{x}_n\right)^2}{2r}+\frac{\cos^3\psi}{1+\cos^3\psi}\frac{\Delta x_n^2}{2r}. \tag{68}$$

Now, we can also write

$$\begin{aligned}\sin\psi&\left(x'-x+\Delta x_n\right)\\ &=\sin\psi\left(x'-x+A\Delta x_n+(1-A)\Delta x_n\right)\\ &=\sin\psi\left(x'-x+\Delta\bar{x}_n\right)+\frac{\sin\psi}{1+\cos^3\psi}\Delta x_n.\end{aligned} \tag{69}$$

Replacing (68) and (69) in (61) leads to (6)–(11).

APPENDIX B

In this appendix, we show how (16) and (17) are obtained, and we compute the range derivative of $\Delta\bar{x}_n$.

First of all, by differentiating (5), we get

$$\begin{aligned}\frac{d\cos\psi}{dr}&=\frac{d^2}{\left(r^2+d^2\right)^{\frac{3}{2}}}=\frac{\sin^2\psi\cos\psi}{r}\\ \frac{d\sin\psi}{dr}&=-\frac{dr}{\left(r^2+d^2\right)^{\frac{3}{2}}}=-\frac{\sin\psi\cos^2\psi}{r}\end{aligned} \tag{70}$$

so that

$$\begin{aligned}\frac{d}{dr}\frac{\sin\psi}{\beta}&=-\frac{\sin\psi\cos^2\psi}{\beta r}\left(1+3\frac{\sin^2\psi\cos\psi}{\beta}\right)\\ \frac{d}{dr}\frac{\cos^3\psi}{\beta}&=\frac{\beta-\cos^3\psi}{\beta^2}3\cos^2\psi\frac{\sin^2\psi\cos\psi}{r}\\ &=3\frac{\sin^2\psi\cos^3\psi}{\beta^2 r}.\end{aligned} \tag{71}$$

By using (71) in differentiating (10), we get

$$\frac{d\Delta r_{\mathrm{an}}}{dr}=\frac{\Delta x_n}{\beta r}\sin\psi\cos^2\psi\left(1+3\frac{\sin^2\psi\cos\psi}{\beta}\right)+ -\frac{\Delta x_n^2}{2\beta r^2}\cos^3\psi\left(1-3\frac{\sin^2\psi}{\beta}\right)\cong\frac{\Delta x_n}{\beta r}\sin\psi\cos^2\psi \tag{72}$$

i.e., (16). In addition, by using the second of (71), we obtain

$$\frac{d\Delta\bar{x}_n}{dr}=3\sin^2\psi\cos^3\psi\frac{\Delta x_n}{\beta^2 r}\cong 3\frac{d^2\Delta x_n}{4r^3}. \tag{73}$$

With regard to (17), we have

$\Delta r_{cn}(x,r)$

$$\cong \Delta r_{cn}(x', r') + \left.\frac{\partial \Delta r_{cn}}{\partial r}\right|_{r=r'} (r - r') + \left.\frac{\partial \Delta r_{cn}}{\partial x}\right|_{x=x'} (x - x') \tag{74}$$

where

$$\begin{aligned}\frac{\partial \Delta r_{cn}}{\partial r} &= -b_n \left[\cos\psi \frac{d\cos(\vartheta_n - \vartheta)}{d\vartheta}\frac{\partial \vartheta}{\partial r} + \frac{d\cos\psi}{dr}\cos(\vartheta_n - \vartheta)\right] \\ &= -b_n \left[\cos\psi \sin(\vartheta_n - \vartheta)\frac{\partial \vartheta}{\partial r} + \frac{\sin^2\psi\cos\psi}{r}\cos(\vartheta_n - \vartheta)\right]\end{aligned} \tag{75}$$

and

$$\begin{aligned}\frac{\partial \Delta r_{cn}}{\partial x} &= -b_n \cos\psi \frac{d\cos(\vartheta_n - \vartheta)}{d\vartheta}\frac{\partial \vartheta}{\partial z}\frac{\partial z}{\partial x} \\ &= -b_n \cos\psi \sin(\vartheta_n - \vartheta)\frac{\partial \vartheta}{\partial z}\frac{\partial z}{\partial x}.\end{aligned} \tag{76}$$

Examination of Fig. 3(b), in which H is the sensor height, leads to

$$r = \frac{H - z}{\cos\vartheta}, \quad \text{i.e., } z = H - r\cos\vartheta \tag{77}$$

from which

$$\begin{aligned}\frac{\partial r}{\partial \vartheta} &= \frac{H - z}{\cos^2\vartheta}\sin\vartheta = r\tan\vartheta \\ \frac{\partial z}{\partial \vartheta} &= r\sin\vartheta.\end{aligned} \tag{78}$$

By using (78) in (75), we get

$$\begin{aligned}\frac{\partial \Delta r_{cn}}{\partial r} &= -\frac{b_n\cos\psi}{r}\left[\frac{\sin(\vartheta_n - \vartheta)}{\tan\vartheta} + \sin^2\psi\cos(\vartheta_n - \vartheta)\right] \cong \\ &\cong -\frac{b_n\cos\psi\sin(\vartheta_n - \vartheta_0)}{r_0\tan\vartheta}\end{aligned} \tag{79}$$

and by using it in (76), we obtain

$$\frac{\partial \Delta r_{cn}}{\partial x} = -\frac{b_n\cos\psi\sin(\vartheta_n - \vartheta)}{r\sin\vartheta}\frac{\partial z}{\partial x}. \tag{80}$$

Use of (79) and (80) in (74) leads to

$$\begin{aligned}\Delta r_{cn}(x, r) \cong \Delta r_{cn}(x', r') &- \frac{b_n\cos\psi\sin(\vartheta_n - \vartheta_0)}{r_0\tan\vartheta}(r - r') \\ &- \frac{b_n\cos\psi\sin(\vartheta_n - \vartheta_0)}{r_0\sin\vartheta}\left.\frac{\partial z}{\partial x}\right|_{x=x'}(x - x').\end{aligned} \tag{81}$$

Finally, (81) coincides with (17) when we let

$$\left.\frac{\partial z}{\partial x}\right|_{x=x'}(x - x') \cong z(x, r') - z(x', r'). \tag{82}$$

Appendix C

In this appendix, we derive (52) and (53).

First of all, we note that maxima and minima of G correspond to minima and maxima of the function

$$L(a_2, \ldots, a_{M-1}) = \left(1 + \chi\sum_{m=2}^{M-1}\frac{1}{a_m} + \chi\right)\left(1 + \sum_{m=2}^{M-1} a_m + \chi\right). \tag{83}$$

Its partial derivatives with respect to a_m are

$$\begin{aligned}\frac{\partial L}{\partial a_m} = -\frac{\chi}{a_m^2}&\left(1 + \sum_{\substack{i=2 \\ i\neq m}}^{M-1} a_i + \chi\right) \\ &+ \left(1 + \chi\sum_{\substack{i=2 \\ i\neq m}}^{M-1}\frac{1}{a_i} + \chi\right) \quad m = 2, \ldots, M-1.\end{aligned} \tag{84}$$

Local maxima or minima of L are obtained by letting

$$\frac{\partial L}{\partial a_m} = 0 \quad m = 2, \ldots, M-1 \tag{85}$$

from which

$$a_m = \sqrt{\chi\left(1 + \chi\sum_{\substack{i=2 \\ i\neq m}}^{M-1}\frac{1}{a_i} + \chi\right)\Bigg/\left(1 + \sum_{\substack{i=2 \\ i\neq m}}^{M-1} a_i + \chi\right)} \quad m = 2, \ldots, M-1. \tag{86}$$

This can be achieved for

$$a_m = \sqrt{\chi} \quad m = 2, \ldots, M-1 \tag{87}$$

as it can be verified by replacing (87) in (86). It can also be verified that the Hessian matrix of L in $a_m = (\chi)^{1/2}$ with $m = 2, \ldots, M-1$ is positive definite so that this is the point of minimum for L and thus the point of maximum for G. By replacing (87) in (50), we get (52).

$$\begin{aligned}&\cos^3\psi\frac{\left(x' - x + A\Delta x_n + (1 - A)\Delta x_n\right)^2}{2r} + \frac{\left(x' - x + A\Delta x_n - A\Delta_{xn}\right)^2}{2r} \\ &= \frac{\cos^3\psi}{2r}\left[\left(x' - x + A\Delta x_n\right)^2 + 2\left(x' - x + A\Delta x_n\right)(1 - A)\Delta x_n + (1 - A)^2\Delta x_n^2\right] \\ &\quad + \left[\left(x' - x + A\Delta x_n\right)^2 - 2\left(x' - x + A\Delta x_n\right)\cdot A\Delta x_n + A^2\Delta x_n^2\right]\end{aligned} \tag{63}$$

There are no other solutions of the system of equations (86) belonging to the allowed domain of variation of a_m. The point of minimum for G will be then one of the vertices of the boundary of the allowed domain of variation of a_m, i.e.,

$$\begin{cases} a_m = 1 \ m = 2, \ldots, k \\ a_m = \chi \ m = k+1, \ldots, M-1 \end{cases} \tag{88}$$

with k integer and $1 \leq k \leq M-1$. By replacing (88) in (50), we get

$$G = N \frac{M^2 \chi}{[M - k + k\chi][k + (M-k)\chi]}. \tag{89}$$

By letting $q = k - M/2$, (89) becomes

$$\begin{aligned} G &= N \frac{M^2 \chi}{\left[\frac{M}{2} - q + \left(\frac{M}{2} + q\right)\chi\right]\left[\left(\frac{M}{2} + q\right) + \left(\frac{M}{2} - q\right)\chi\right]} \\ &= N \frac{M^2 \chi}{\left[\frac{M}{2}(1+\chi) + q(\chi - 1)\right]\left[\frac{M}{2}(1+\chi) - q(\chi - 1)\right]} \\ &= N \frac{4\chi}{\left[(1+\chi)^2 - \frac{4q^2}{M^2}(\chi - 1)^2\right]}. \end{aligned} \tag{90}$$

This quantity assumes its minimum value when q^2 attains its minimum allowed value, which is zero for M even, and 1/4 for M odd, so obtaining the expressions in (53).

REFERENCES

[1] G. Franceschetti and R. Lanari, *Synthetic Aperture Radar Processing*. Boca Raton, FL, USA: CRC Press, 2018.

[2] A. Moreira, P. Prats-Iraola, M. Younis, G. Krieger, I. Hajnsek, and K. P. Papathanassiou, "A tutorial on synthetic aperture radar," *IEEE Geosci. Remote Sens. Mag. Replaces Newsletter*, vol. 1, no. 1, pp. 6–43, Mar. 2013.

[3] G. Soldi et al., "Space-based global maritime surveillance. Part I: Satellite technologies," *IEEE Aerosp. Electron. Syst. Mag.*, vol. 36, no. 9, pp. 8–28, Sep. 2021.

[4] A. Renga, M. D. Graziano, and A. Moccia, "Formation flying SAR: Analysis of imaging performance by array theory," *IEEE Trans. Aerosp. Electron. Syst.*, vol. 57, no. 3, pp. 1480–1497, Jun. 2021.

[5] G. Krieger and A. Moreira, "Spaceborne bi- and multistatic SAR: Potential and challenges," *IEE Proc. Radar, Sonar Navig.*, vol. 153, no. 3, pp. 184–198, 2006.

[6] J. Paul Aguttes, "The SAR train concept: An along-track formation of SAR satellites for diluting the antenna area over smaller satellites, while increasing performance by," *Acta Astronautica*, vol. 57, nos. 2–8, pp. 197–204, Jul. 2005.

[7] D. Cerutti-Maori, I. Sikaneta, J. Klare, and C. H. Gierull, "MIMO SAR processing for multichannel high-resolution wide-swath radars," *IEEE Trans. Geosci. Remote Sens.*, vol. 52, no. 8, pp. 5034–5055, Aug. 2014.

[8] N. Gebert, G. Krieger, and A. Moreira, "Digital beamforming on receive: Techniques and optimization strategies for high-resolution wide-swath SAR imaging," *IEEE Trans. Aerosp. Electron. Syst.*, vol. 45, no. 2, pp. 564–592, Apr. 2009.

[9] G. Krieger et al., "MirrorSAR: A fractionated space radar for bistatic, multistatic and high-resolution wide-swath SAR imaging," in *Proc. IEEE Int. Geosci. Remote Sens. Symp. (IGARSS)*, Fort Worth, TX, USA, Jul. 2017, pp. 149–152.

[10] N. A. Goodman and J. M. Stiles, "Resolution and synthetic aperture characterization of sparse radar arrays," *IEEE Trans. Aerosp. Electron. Syst.*, vol. 39, no. 3, pp. 921–935, Jul. 2003.

[11] C. Prati and F. Rocca, "Improving slant-range resolution with multiple SAR surveys," *IEEE Trans. Aerosp. Electron. Syst.*, vol. 29, no. 1, pp. 135–143, Jan. 1993.

[12] P. Lopez-Dekker, G. Krieger, and A. Moreira, "Multistatic radar system," in *Distributed Space Missions for Earth System Monitoring*, M. D'Errico, Ed. New York, NY, USA: Springer, 2013, pp. 61–122.

[13] S. Duque, C. Rossi, and T. Fritz, "Single-pass tomography with alternating bistatic TanDEM-X data," *IEEE Geosci. Remote Sens. Lett.*, vol. 12, no. 2, pp. 409–413, Feb. 2015.

[14] S. V. Baumgartner and G. Krieger, "Dual-platform large along-track baseline GMTI," *IEEE Trans. Geosci. Remote Sens.*, vol. 54, no. 3, pp. 1554–1574, Mar. 2016.

[15] G. di Martino et al., "Formation-flying SAR receivers in FAR-from-transmitter geometry: X-band SAR antenna design," in *Proc. IEEE Int. Geosci. Remote Sens. Symp. (IGARSS)*, Jul. 2021, pp. 2723–2726.

[16] P. Guccione, A. Monti Guarnieri, F. Rocca, D. Giudici, and N. Gebert, "Along-track multistatic synthetic aperture radar formations of minisatellites," *Remote Sens.*, vol. 12, no. 1, p. 124, Jan. 2020.

[17] G. Krieger, N. Gebert, and A. Moreira, "Unambiguous SAR signal reconstruction from nonuniform displaced phase center sampling," *IEEE Geosci. Remote Sens. Lett.*, vol. 1, no. 4, pp. 260–264, Oct. 2004.

[18] I. Sikaneta, C. H. Gierull, and D. Cerutti-Maori, "Optimum signal processing for multichannel SAR: With application to high-resolution wide-swath imaging," *IEEE Trans. Geosci. Remote Sens.*, vol. 52, no. 10, pp. 6095–6109, Oct. 2014.

[19] P. Cheng, J. Wan, Q. Xin, Z. Wang, M. He, and Y. Nian, "An improved azimuth reconstruction method for multichannel SAR using Vandermonde matrix," *IEEE Geosci. Remote Sens. Lett.*, vol. 14, no. 1, pp. 67–71, Jan. 2017.

[20] G. Krieger and M. Younis, "Impact of oscillator noise in bistatic and multistatic SAR," *IEEE Geosci. Remote Sens. Lett.*, vol. 3, no. 3, pp. 424–428, Jul. 2006.

[21] M. Rodriguez-Cassola, P. Prats-Iraola, P. Lopez-Dekker, A. Reigber, G. Krieger, and A. Moreira, "Autonomous time and phase calibration of spaceborne bistatic SAR systems," in *Proc. 10th Eur. Conf. Synth. Aperture Radar*, Jun. 2014, pp. 1–4.

[22] M. D. Graziano, A. Renga, M. Grasso, and A. Moccia, "Error sources and sensitivity analysis in formation flying synthetic aperture radar," *Acta Astronautica*, vol. 192, pp. 97–112, Mar. 2022.

[23] M. Grasso, A. Renga, G. Fasano, M. D. Graziano, M. Grassi, and A. Moccia, "Design of an end-to-end demonstration mission of a formation-flying synthetic aperture radar (FF-SAR) based on microsatellites," *Adv. Space Res.*, vol. 67, no. 11, pp. 3909–3923, Jun. 2021.

[24] G. Krieger, N. Gebert, and A. Moreira, "SAR signal reconstruction from non-uniform displaced phase centre sampling," in *Proc. IEEE Int. Geosci. Remote Sens. Symp. (IGARSS)*, vol. 3, Jun. 2004, pp. 1763–1766.

[25] M. D. Graziano, A. Renga, M. Grasso, and A. Moccia, "PRF selection in formation-flying SAR: Experimental verification on Sentinel-1 monostatic repeat-pass data," *Remote Sens.*, vol. 12, no. 1, p. 29, Dec. 2020.

[26] A. Renga, M. D. Graziano, M. Grasso, and A. Moccia, "Timing and design issues in formation flying distributed SAR," in *Proc. IEEE Radar Conf. (RadarConf)*, Sep. 2020, pp. 1–6.

[27] V. A. Marčenko and L. A. Pastur, "Distribution of eigenvalues for some sets of random matrices," *Math. USSR-Sbornik*, vol. 1, no. 4, pp. 457–483, Apr. 1967.

Gerardo Di Martino (Senior Member, IEEE) was born in Naples, Italy, in 1979. He received the Laurea degree (cum laude) in telecommunication engineering and the Ph.D. degree in electronic and telecommunication engineering from the University of Naples Federico II, Naples, in 2005 and 2009, respectively.

From 2009 to 2016, he was with the University of Naples Federico II, working on projects regarding applied electromagnetics and remote sensing topics. From 2014 to 2015, he was with the Italian National Consortium for Telecommunications (CNIT), Naples. In 2016, he was also with the Regional Center Information Communication Technology (CeRICT), Naples. He is currently an Associate Professor of electromagnetics with the Department of Electrical Engineering and Information Technology, University of Naples Federico II. His research interests include microwave remote sensing and electromagnetics, with a focus on electromagnetic scattering from natural surfaces and urban areas, synthetic aperture radar (SAR) signal processing and simulation, information retrieval from SAR data, and electromagnetic propagation in urban areas.

Prof. Di Martino is an Associate Editor of IEEE JOURNAL OF SELECTED TOPICS ON APPLIED EARTH OBSERVATIONS AND REMOTE SENSING, IEEE ACCESS, *Remote Sensing* (MDPI), and *Electronics* (MDPI).

Alessio Di Simone (Member, IEEE) was born in Torre del Greco, Italy, in 1989. He received the B.Sc. and M.Sc. Laurea degrees (cum laude) in telecommunication engineering and the Ph.D. degree in information technology and electrical engineering from the University of Naples Federico II, Naples, Italy, in 2011, 2013, and 2017, respectively.

In 2016, he joined the Universitat Politècnica de Catalunya, Barcelona, Spain, as a Visiting Researcher. In 2017, 2018, and 2023, he was a Visiting Researcher with the NATO Science and Technology Organization Centre for Maritime Research and Experimentation (CMRE), La Spezia, Italy. From 2017 to 2021, he was a Research Fellow with the Department of Electrical Engineering and Information Technology, University of Naples Federico II, where he has been an Assistant Professor of electromagnetic fields since 2022. His main research interests are in the field of microwave remote sensing and electromagnetics including modeling of the electromagnetic scattering from natural surfaces, urban areas, and artificial targets, and simulation and processing of synthetic aperture radar (SAR) and Global Navigation Satellite System Reflectometry (GNSS-R) data.

Dr. Di Simone received the Prize for the Best Master Thesis in Remote Sensing by the IEEE South Italy Geoscience and Remote Sensing Chapter in 2015 and the 2022 Best Young Researcher in Oceanic Engineering Award from the IEEE Oceanic Engineering Italy Chapter.

Antonio Iodice (Senior Member, IEEE) was born in Naples, Italy, in 1968. He received the Laurea degree (cum laude) in electronic engineering and the Ph.D. degree in electronic engineering and computer science from the University of Naples Federico II, Naples, in 1993 and 1999, respectively.

In 1995, he joined the Research Institute for Electromagnetism and Electronic Components of the Italian National Council of Research (IRECE-CNR), Naples. From 1999 to 2000, he was with Telespazio S.p.A., Rome, Italy. From 2000 to 2004, he was a Research Scientist with the University of Naples Federico II, where he was a Professor of Electromagnetics from 2005 to 2018. He is currently a Full Professor of Electromagnetics with the Department of Electrical Engineering and Information Technology, University of Naples Federico II, where he is also the Coordinator of the B.S. and M.S. degree programs in telecommunications and digital media engineering. He has been involved as a Principal Investigator or a Co-Investigator in several projects funded by European Union (EU), Italian Space Agency (ASI), Italian Ministry of Education and Research (MIUR), Campania Regional Government, and private companies. He has authored or coauthored two books and more than 350 articles, of which over 100 published on refereed journals. His main research interests are in the field of microwave remote sensing and electromagnetics, modeling of electromagnetic scattering from natural surfaces and urban areas, simulation and processing of synthetic aperture radar (SAR) signals, and electromagnetic propagation in urban areas.

Prof. Iodice received the 2009 Sergei A. Schelkunoff Transactions Prize Paper Award from the IEEE Antennas and Propagation Society, for the best paper published in 2008 on the IEEE TRANSACTIONS ON ANTENNAS AND PROPAGATION. He was recognized by the IEEE Geoscience and Remote Sensing Society as a 2015 Best Reviewer of the IEEE TRANSACTIONS ON GEOSCIENCE AND REMOTE SENSING. He is the Past Chair of the IEEE Geoscience and Remote Sensing South Italy Chapter.

Daniele Riccio (Fellow, IEEE) was born in Naples, Italy. He received the Laurea degree (cum laude) in electronic engineering from the University of Naples Federico II, Naples, in 1989.

He was a Research Scientist with the Italian National Research Council, Institute for Research on Electromagnetics and Electronic Components, Naples, from 1989 to 1994, a Guest Scientist with the German Aerospace Centre (DLR), Munich, Germany, from 1994 to 1995, and a Research Affiliate with the National Aeronautics and Space Administration (NASA), Washington, DC, USA, from 2010 to 2018. He lectured abroad (Spain and Czech Republic) in Ph.D. Schools. He is a member of the Cassini Radar Science Team and the Italian Space Agency Platino-1 Mission Advisory Group. His career has been developing at the University of Naples Federico II, where he is currently a Full Professor of electromagnetic fields with the Department of Electrical Engineering and Information Technology and the Rector Delegate for Ph.D. Schools, and coordinates the Ph.D. School in Information and Communication Technology for Health. He is a Board Member for the Ph.D. Program on Space at the Scuola Superiore Meridionale, Naples. He is a member of the Board of Directors for the RESTART Foundation, Rome, Italy, in charge of the Telecommunications of the Future PNRR Program and the Director of the CNIT National Laboratory on Multimedia Telecommunication, Napoli. He has authored four books and 500 scientific articles. His research interests include electromagnetic theory, remote sensing, electromagnetic scattering from complex media and surfaces, synthetic aperture radar techniques, application of fractal geometry to remote sensing, and propagation of electromagnetic fields for wireless communication networks planning.

Prof. Riccio was a recipient of the 2009 Sergei A. Schelkunoff Transactions Prize Paper Award for the best paper published in 2008 on the IEEE TRANSACTIONS ON ANTENNAS AND PROPAGATION. He has been the General Chair of the 5G International Ph.D. School since 2018. He is an associate editor of some journals on remote sensing. He is the Athenaeum Representative with the Italian Society of Electromagnetism (SIEm), where he is a member of the Board of Directors appointed with the Secretary role.

Giuseppe Ruello (Senior Member, IEEE) was born in Naples, Italy, in 1975. He received the Laurea degree (cum laude) in telecommunication engineering and the Ph.D. degree in information engineering from the University of Naples Federico II, Naples, in 1999 and 2003, respectively.

In 2019, he joined the Department of Radiology, New York University, New York, NY, USA, as a Fulbright Scholar. In 2002 and from 2004 to 2005, he was a Visiting Scientist with the Department of Signal Theory and Communications, Universitat Politecnica de Catalunya of Barcelona, Barcelona, Spain. He is currently an Associate Professor with the Department of Electrical Engineering and Information Technology, University of Naples Federico II. He has authored or coauthored more than 200 articles, of which over 50 published on refereed journals. His main research interests include synthetic aperture radar (SAR) remote sensing, modeling of electromagnetic scattering from natural surfaces, fractal models, SAR raw signal simulation, modeling of electromagnetic field propagation in urban environment, modeling of radio frequency field in magnetic resonance, and remote sensing techniques for low-income semiarid regions.

Open Access funding provided by 'Università degli Studi di Napoli "Federico II"' within the CRUI CARE Agreement